PERIODICALLY POLED LITHIUM NIOBATE: MODELING, FABRICATION, AND NONLINEAR-OPTICAL PERFORMANCE

A DISSERTATION

SUBMITTED TO THE DEPARTMENT OF ELECTRICAL ENGINEERING

AND THE COMMITTEE ON GRADUATE STUDIES

OF STANFORD UNIVERSITY

IN PARTIAL FULFILLMENT OF THE REQUIREMENTS

FOR THE DEGREE OF

DOCTOR OF PHILOSOPHY

Gregory David Miller

July 1998

I certify that I have read this dissertation and that in my opinion it is fully adequate, in scope and quality, as a dissertation for the degree of doctor of Philosophy.

Robert L. Byer

I certify that I have read this dissertation and that in my opinion it is fully adequate, in scope and quality, as a dissertation for the degree of doctor of Philosophy.

Stephen E. Harris

I certify that I have read this dissertation and that in my opinion it is fully adequate, in scope and quality, as a dissertation for the degree of doctor of Philosophy.

Martin M. Fejer

I certify that I have read this dissertation and that in my opinion it is fully adequate, in scope and quality, as a dissertation for the degree of doctor of Philosophy.

Umran S. Inan

Approved for the University Committee on Graduate Studies:

Abstract

Periodically poled lithium niobate (PPLN) has become the nonlinear-optical material of choice in many infrared optical parametric oscillators (OPO's) due to its high nonlinearity, readily engineered tuning characteristics, and repeatable fabrication. The domain periods required for these OPO's are typically between 15 µm and 30 µm, and are made by a process already well developed. The domain periods required for visible light applications are typically between 3 µm and 10 µm, and are more difficult to fabricate repeatably. The focus of this research was to understand the nature of this difficulty, to develop strategies for repeatable device fabrication, and to demonstrate the nonlinear optical performance of the material.

This thesis presents a model of the periodic-poling process in lithium niobate, a repeatable PPLN-fabrication process developed using this model, and the nonlinear-optical performance of PPLN fabricated with this process. The model combines ferroelectric properties of the material, measured as part of this research, with the electrostatics of periodic electrodes. The fabrication process developed using the model was used to periodically pole two 75-mm-diameter wafers of 500-µm-thick $LiNbO_3$ with a 6.5 µm domain period. These wafers yielded 53-mm-long samples, more than five times the length previously reported. Second harmonic generation experiments performed with these samples produced 2.7 watts of 532 nm radiation output with 6.5 watts of continuous-wave 1064 nm Nd:YAG laser radiation input, corresponding to a record 42% single-pass conversion efficiency. These samples were also used to operate the first reported continuous-wave 532-nm-pumped PPLN-based singly-resonant OPO, with a record-low 0.93-watt threshold (relative to other 532-nm-pumped OPO's), 56% conversion efficiency, and continuous tuning from 917-1266 nm. Finally, data are presented that indicate the presence of 532-nm-induced 1064-nm absorption.

Acknowledgements

I would not have been able to complete this thesis without the support of numerous individuals and institutions. So great is the number in fact that I fear I may fail to recognize all who have contributed to this effort, but in gratitude I attempt to do so here.

Professor Robert Byer has a gift for seeing the potential in a person even before they see it in themselves, as was the case with me. His patience, optimism, excitement for the work, and frequent encouragement inspired me to stay true to my objectives despite various adversities.

Professor Marty Fejer was often available to me, contributing new perspectives, asking probing questions, and generally providing a sounding board for my ideas. Many times the light under his door could be seen until the early morning hours, and a knock would always result in a reply of, “Come in!”

Both Professors Byer and Fejer contributed financially to my research by permitting me to purchase time, materials, and equipment. I thank them for their tireless fund raising efforts.

Professor Stephen Harris was my academic advisor and was helpful a number of times throughout my academic program. Molly Sandperl-Black, Dr. Jerome Elkind, Dennis Mathies, and the students at the Disability Resource Center also provided much-needed assistance, especially in my first few years at Stanford. Kellie Koucky is Professor Byer’s energetic and caring secretary, and I thank her for her efforts to facilitate everything from expense reports to the growth of spirituality.

I thank Dr. Jack Olin for suggesting to me in 1989 that I might consider applying for a General Motors Fellowship to graduate school. He was an inspiration to me as a Professor at General Motors Institute and then as the Department Head of Advanced Engineering at Packard Electric Division. Together with Jim Orsine, Bob Steele, and Rudy Schlais, they made possible this educational experience. I also thank General Motors for their support through the Fellowship Program.

I am grateful to Lightwave Electronics and the Center for Nonlinear Optical Materials for their direct financial support during my last year as a graduate student. Thanks also to Silicon Light Machines for their role in helping me complete this dissertation after becoming a new employee.

The services of Ginzton Laboratory were essential to the completion of this work. I thank Ted Bradshaw for giving me the skills I needed in the machine shop, Tom Carver for acting as my Clean Room coach and trainer, and Joe Vrehl and Chris Remen for their world-class work in crystal fabrication.

I found the Stanford experience unique not only for its academics and research, but also for its ability to attract the very best students in the world. Ginzton Laboratory seems particularly gifted in this regard. I am thankful especially to those students with whom I most closely worked for their friendship and selfless contribution to my work. Mike Bortz taught me all the fine points of $LiNbO_3$ processing. Larry Myers shared many hours and countless ideas with me as we grew in knowledge of the poling process. Rob Batchko worked with me to produce ever-shorter domain periods and worked tirelessly to see both poling and optical experiments to their end. Mark Arbore was a source of frequent consultations that contributed to this work. Bill Tulloch gave generously of his laser knowledge and time to help me achieve the optical performance reported in this thesis.

To my parents, relatives, and in-laws with whom my family and I could only connect by telephone for the time I've spent here at Stanford, I've missed you, and I thank you for the tremendous faith you've placed in me.

To my children David, Christopher, and Andrea, I give my eternal love and gratitude. You grew up for the most part in Escondido Village and went days at a time waiting for me to come home from the lab. You gave many weekends to me to help me realize my dream.

Finally, to my wife Cathi, I thank you for believing in me from the beginning, for believing in our ability to work together as a couple and as a family toward this goal, for your seemingly endless patience and understanding, and for loving me no matter what. I will love you until the end of time.

Table of Contents

List of Tables

List of Illustrations

CHAPTER 1. INTRODUCTION

1.1. Motivation

The research for this dissertation began with a quest to develop highly efficient and economical multi-watt red, green, and blue lasers for display applications. It was apparent that semiconductor lasers would not be available for many years to come at power levels and at wavelengths suitable for display applications. The alternative was to convert the wavelengths of currently available lasers to those required for displays using nonlinear optics, a technology extensively described in the literature (see for example the works by Bloembergen[1] and Akhmanov and Khokhlov[2]). Nonlinear optics has been used to produce wavelengths throughout the visible spectrum, over a wide range of powers, with optical-to-optical efficiencies as high as 65%[3]. However, the relatively low nonlinear coefficient of available materials required researchers to employ resonant or mode-locked frequency conversion schemes that were incompatible with the economics of displays, or to use nonlinear waveguides that had limitations in power handling capability. To meet the needs of display applications, a new class of nonlinear optical materials employing quasi-phase-matching[4] would be required, and their development became the focus of this research.

After a brief description of the light source requirements for displays, the requirements on the nonlinear optical material are presented. The strategy for material development is then discussed. The central contributions of this research are listed, followed with an overview of this dissertation.

1.2. A laser source for displays

Displays for consumer applications require reliable multi-watt sources that can be manufactured in high volumes for less than $100/watt. Although many factors influence manufacturing costs, some of the most significant are the number of parts and alignment steps, tight tolerances, and the cost of components. To reduce the number of parts and

alignment steps, a bulk single-pass configuration for second harmonic generation (SHG) using one infrared semiconductor laser and one nonlinear crystal, shown schematically in Figure 1.1, is preferred over a resonant design. Bulk frequency conversion is also preferred over waveguides, depending on the available laser power, to avoid tight tolerances. Should waveguides be needed for adequate conversion efficiency however, tapering[5] can be used to relax positional alignment tolerances.

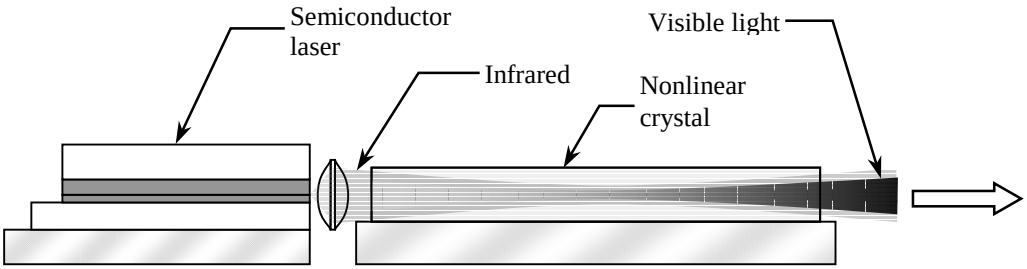

Figure 1.1. Schematic of bulk single-pass second harmonic visible light generator

Of the various components in this source, the semiconductor laser and nonlinear crystal are the costliest. Semiconductor laser prices have declined at approximately 30%/year since 1985[6], and laser bars are currently under $100/watt. Because of the sensitivity of price to volume in the semiconductor industry, prices should continue to fall. Single-emitter multi-watt semiconductor lasers are expected to follow a price-volume relationship similar to that of laser bars. Like the semiconductor laser, the cost of the nonlinear crystal is also strongly tied to volume and the stability of the fabrication technology. Consequently, it is more reasonable to seek out ways to modify existing nonlinear optical materials than to develop altogether new crystals. $LiNbO_3$, often referred to as "the silicon of nonlinear optics," is an excellent candidate for this application because of the following reasons: First, $LiNbO_3$ is already produced at a volume of 40 tons per year for consumer applications (cellular phones and televisions) using a very stable fabrication technology. Second, $LiNbO_3$ is transparent from 350 nm to 5000 nm, providing low loss for both the fundamental and harmonic for visible light generation. Finally, $LiNbO_3$ has nonlinear coefficients for visible light generation among the highest of all inorganic materials. Rather than seeking to discover and develop a new nonlinear material, this research was directed toward improving $LiNbO_3$ in such a way as to maximize its utility for red, green, and blue light generation.

1.3. Requirements for the nonlinear crystal

The conversion efficiency of the nonlinear crystal has an impact on the total system cost by affecting the power requirements of the semiconductor laser source. A reasonable goal for single-pass conversion efficiency is that it should exceed 25% to avoid excessive laser cost. In the low conversion limit, conversion efficiency η for confocal focusing is given by

$$\eta \equiv \frac{P_{2\omega}}{P_{\omega}} = 16\pi^2 \frac{d_{eff}{}^2 Z_o}{n_{\omega} n_{2\omega} \lambda^3} L P_{\omega} \mathrm{sinc}^2\left[\Delta k L/2\right], \tag{1.1}$$

where $P_{2\omega}$ is the power in the second harmonic, P_{ω} is the power in the fundamental, d_{eff} is the effective nonlinear coefficient in m/volt, Z_o is the impedance of free space, $\Delta k \equiv k_{2\omega} - 2k_{\omega}$, $k_{2\omega} \equiv 2\pi n_{2\omega}/(\lambda/2)$, $n_{2\omega}$ is the index of refraction at the harmonic, $k_{\omega} \equiv 2\pi n_{\omega}/\lambda$, n_{ω} is the index of refraction at the fundamental, λ is the fundamental wavelength, L is the length of the nonlinear crystal, and

$$\mathrm{sinc}(x) \equiv \frac{\sin(x)}{x}.$$

Note that conversion efficiency is proportional to crystal length, input power, and the square of the effective nonlinear coefficient. As crystal length is increased, conversion efficiency increases, but the nonlinear conversion process becomes more sensitive to changes in wavelength, temperature, strain, and other factors affecting the difference in refractive indices. In addition to overall variation in the refractive index difference, local variations impose an additional constraint on the maximum useful crystal length. As a result, length alone cannot be used to compensate for either low nonlinearity or low input power.

To estimate the nonlinearity required to produce one watt of 532 nm green light from a four-watt 1064 nm source, consider an example where the nonlinear material has refractive indices of approximately 2 at both the fundamental and harmonic, and the maximum device length is limited to 50 mm. Solving Equation (1.1) for d_{eff},

$$d_{eff} = 10\,\mathrm{pm/volt}.$$

This nonlinearity produces a normalized conversion efficiency of 1.25%/(watt·cm). Sources based on bulk single-pass second harmonic generation therefore require crystals

with a nonlinear coefficient greater than 10 pm/volt, useful lengths up to 50 mm, and good transparency throughout the visible range. While crystals exist that satisfy two out of three of these requirements, there were none prior to this research capable of satisfying all three simultaneously.

1.4. Strategy for material development

While $LiNbO_3$ is an attractive material because of its status as a commodity material, the only component of its nonlinear tensor large enough to satisfy the requirements of display applications is d_{33}, having a value of 25.2 pm/volt[7]. While dispersion prevents direct access to the full d_{33} coefficient, quasi-phase-matching (QPM) can provide up to 64% of the full nonlinearity, or 16 pm/volt, making $LiNbO_3$ a very strong candidate for display applications.

The theory of QPM, first described by Armstrong, *et al.*[4] in 1962 and by Franken and Ward[8] in 1963, has been discussed and extended by numerous authors. Essentially it is a technique that compensates for the difference in phase velocity between the fundamental wave and its harmonic in a nonlinear crystal caused by natural dispersion. This approach is fundamentally different from birefringent phase matching[4], where the anisotropy of nonlinear crystal is used to find unique propagation directions whereby the fundamental and harmonic waves have the same phase velocity. In QPM, the two waves are allowed to have different phase velocities, and they shift π out of phase relative to one another over a distance called the coherence length. The sign of the nonlinear coefficient is reversed every coherence length, causing the locally generated harmonic field to transfer power to the harmonic beam. By compensating for phase-velocity mismatch in this way, all elements of a crystal's nonlinear tensor can be accessed throughout the entire transparency range.

The formula for conversion efficiency η_Q for QPM with confocal focusing is similar to Equation (1.1), with terms added to account for phase-velocity mismatch compensation and the reduction of the nonlinear coefficient by the periodic modulation of its sign. η_Q is given by

$$\eta_Q = 16\pi^2 \frac{{d_m}^2 Z_o}{n_\omega n_{2\omega} \lambda^3} L P_\omega \mathrm{sinc}^2\left[\Delta k_Q L/2\right], \tag{1.2}$$

where

$$d_m \equiv \frac{2}{m\pi}\sin(m\pi D)\, d_{eff}\,.$$

d_m is the effective nonlinearity of the mth harmonic of the QPM grating, D is the duty cycle of the grating (coherence length divided by grating period), $\Delta k_Q \equiv \Delta k - K_m$, $K_m \equiv 2\pi m/\Lambda$, and Λ is the grating period.[9] Because of QPM, it is possible to use $LiNbO_3$ to create viable bulk single-pass light sources for display applications, since it provides a way to obtain a normalized room temperature conversion efficiency of 2.6%/(watt·cm) for 1064 nm SHG, nearly twice the minimum requirement. For SHG of 852 nm to generate 426 nm blue, the normalized conversion efficiency is 5.2%/(watt·cm), four times larger than the minimum requirement.

Two other potential materials in which QPM has been demonstrated for visible light generation are $LiTaO_3$ and $KTiOPO_4$ (KTP). $LiTaO_3$ has a normalized room temperature conversion efficiency of 0.83%/(watt·cm), below that required for bulk single-pass 1064 nm SHG. However, for 852 nm SHG, $LiTaO_3$ has a normalized conversion efficiency of 1.8%/(watt·cm) and would be suitable for that application. KTP has a normalized conversion efficiency for 1064 nm SHG of 1.7 %/(watt·cm). To achieve 25% single-pass conversion efficiency of a one watt fundamental, a crystal of 3.6-cm length is required; however, the maximum crystal length in production is 3 cm. For 852 nm SHG, KTP's normalized conversion efficiency is 4.1%/(watt·cm), and would be a strong candidate for that application.

To create QPM structures in these and other materials, various approaches have been studied, including use of rotationally twinned crystals, stacking of alternately oriented thin plates, and growth of periodic domain structures in ferroelectrics.[10] For waveguides where QPM is required only at the surface of the crystal, periodic annihilation of the nonlinear coefficient[11] and periodic domain inversion by dopant indiffusion in ferroelectrics[12,13] have been employed. Most recently, numerous researchers have studied bulk periodic domain formation in ferroelectrics by applying an electric field using lithographically defined periodic electrodes. Yamada, *et al*. was the first to have reported a demonstration of this approach[14]. This last technique is referred to as electric field

periodic poling, and is now often referred to simply as periodic poling. ("Poling" refers to the process whereby the spontaneous polarization of a ferroelectric crystal can be reversed under the influence of a sufficiently large electric field. In this dissertation, the term "electric field periodic poling" will be used to differentiate from other periodic poling techniques.) Reviews of progress in QPM are available in References 9, 15, and 16.

The two waveguide techniques and electric field periodic poling all share a common and important feature in their implementation. In all three cases, lithographic techniques are used to assure the periodicity of the QPM structure, where even small errors in periodicity can substantially degrade conversion efficiency.[9] The fabrication of masks used in lithography employs interferometric feedback control, limiting the positional error of any feature over the dimension of the mask to less than a quarter-wavelength of He-Ne radiation, or 0.16 µm. For a 5-cm-long 5-µm-period grating, this amounts to a maximum period fluctuation of 6 parts in 1 million, resulting in a negligible reduction in conversion efficiency. The ability to define QPM structures with lithographic precision created an opportunity in nonlinear optics to fabricate devices with interaction lengths not possible using non-lithographic techniques.

The strategy for material development was to advance the technology of bulk electric field periodic poling in $LiNbO_3$ so that 50-mm-long, 0.5-mm-thick devices with at least 50% of the ideal first-order QPM nonlinear coefficient could be routinely fabricated with good uniformity over an entire 75-mm-diameter wafer. $LiTaO_3$ was not chosen because it lacked sufficient nonlinearity for green light generation. KTP was not chosen because it was not available in sufficiently long devices, was prohibitively expensive, and suffered from a number of quality issues. It was necessary to extend electric field periodic poling technology to allow domain periods for visible light generation to be produced as readily as periods 15 µm[17] and greater; 50-mm-long, 0.5-mm-thick periodically poled $LiNbO_3$ (PPLN) with a 29.75-µm period was reported in 1996[18]. Domain periods between 6 µm and 7 µm are required for green light generation, and blue light generation requires domain periods between 4 µm and 5 µm. Prior to the completion of this research, the longest PPLN devices produced for visible light had a

period of 4.6 µm, were 6 mm long, and were produced in samples 200 µm thick.[19] Domain pattern quality grew increasingly difficult as the period was reduced.

It was necessary to develop and verify a model of the electric field poling process that accounted for the dependence of domain quality on period and thickness in order to find a means for producing shorter domain periods. At the same time, new fabrication methods and materials were needed in order to implement the findings of the model.

1.5. The central contributions of this research

This research produced a model of the electric field periodic poling process in $LiNbO_3$ that predicts poling outcomes and is useful as a design tool. The model taught that the insulator used to cover the electrodes and the spaces between them, the interface between the insulator and the $LiNbO_3$ surface, and the near-surface region of the $LiNbO_3$ all had to have low conductivity and high dielectric strength. Conductivity between the electrodes was found to be a significant contributor to the loss of domain pattern quality as domain period is reduced and substrate thickness is increased. The fabrication technology developed in the course of this research showed that spin-on-glass was capable of providing adequate dielectric strength and low conductivity.

The model also taught that domain nucleation site density must increase with the inverse-square of the domain period and have a value on the order of one domain per period-squared in order to maintain domain pattern quality. Experiments showed that the choice of electrode material had a large effect on nucleation site density and also found that sputtered nichrome produced enough nuclei per unit area to permit fabrication of visible light devices.

This dissertation also contributes new data showing the relationship between the growth rate of domains and the applied poling field in $LiNbO_3$, and it teaches how this data can be used to design an optimized poling waveform. This data was combined with the electrostatics of periodic poling, also developed for this research, to generate an equation of domain wall motion during electric field periodic poling.

As a result of this research, 75-mm-diameter wafers of 0.5-mm-thick $LiNbO_3$ were poled with a 6.5 µm domain period, producing samples 53-mm long.[20] These samples quasi-phase-matched over their entire length and were the longest periodically poled

devices ever made for second harmonic generation of visible light. The samples had an effective nonlinear coefficient of 14 pm/volt, and had an overall normalized conversion efficiency of 8.5%/watt, the largest ever reported for bulk cw single-pass operation. The samples were used to produce internally 2.7 watts of 532-nm second harmonic from 6.5 watts of 1064-nm internal cw input, indicating an optical-to-optical conversion efficiency of 42%. Both the cw power and conversion efficiency were the highest ever reported for a bulk single-pass configuration.

The samples were also used to produce the first cw 532-nm-pumped singly resonant optical parametric oscillator (SRO) based on QPM. Using a four-mirror ring cavity and single-pass pumping, the SRO had a sub-watt internal oscillation threshold, 56% quantum efficiency and tuned from 917 nm to 1266 nm.

1.6. Overview of dissertation

Chapter 2 presents a model of domain kinetics during electric field periodic poling, provides experimental support for the model, and shows how this model was used to fabricate PPLN with a 6.5 μm domain period. Chapter 3 discusses the nonlinear-optical performance of the samples described in Chapter 2, giving experimental results for both second harmonic generation and SRO operation. Chapter 4 concludes this dissertation and provides suggestions for future work. Appendix A presents the electrostatics of electric field periodic poling and techniques for efficient computation of electric field, surface charge density, domain wall position, and domain wall velocity. Appendix B provides the interested reader with Mathcad 7.0 functions that can speed implementation of the electrostatics formulas.

References for Chapter 1

1 N. Bloembergen, "Nonlinear Optics," Benjamin, New York (1965).

2 S. A. Akhmanov and R. V., "Problems in Nonlinear Optics," Akad. Nauk. USSR, Moscow (1964). English edition, Gordon and Breach, New York (1973).

3 D. C. Gerstenberger, G. E. Tye, and R. W. Wallace, "Efficient second-harmonic conversion of CW single-frequency Nd:YAG laser light by frequency locking to a monolithic ring frequency doubler," Optics Letters **16** (13), 992-4 (1991).

4 J. A. Armstrong, N. Bloembergen, J. Ducuing, and P. S. Pershan, "Interactions between light waves in a nonlinear dielectric," Phys. Rev. **127**, 1918 (1962).

5 M. H. Chou, M. A. Arbore, and M. M. Fejer, "Adiabatically tapered periodic segmentation of channel waveguides for mode-size transformation and fundamental mode excitation," Optics Letters **21** (11), 794-6 (1996).

6 Semiconductor laser price data accumulated by R. L. Byer, Stanford University.

7 I. Shoji, T. Kondo, A. Kitamoto *et al*., "Absolute scale of second-order nonlinear-optical coefficients," Journal of the Optical Society of America B (Optical Physics) **14** (9), 2268-94 (1997).

8 P. A. Franken and H. F. WARD, "Optical harmonics and nonlinear phenomena," *Rev. Mod. Phys*., **35**, PP. 23-39 (1963).

9 M. M. Fejer, G. A. Magel, D. H. Jundt *et al*., "Quasi-phase-matched second harmonic generation: tuning and tolerances," IEEE Journal of Quantum Electronics **28** (11), 2631-2654 (1992).

10 See references in Fejer, *et al.*, IEEE Journal of Quantum Electronics **28** (11), 2631-2654 (1992).

11 J. D. Bierlein, D. B. Laubacher, J. B. Brown *et al*., "Balanced phase matching in segmented $KTiOPO_4$ waveguides," Applied Physics Letters **56** (18), 1725-7 (1990).

12 E. J. Lim, M. M. Fejer, and R. L. Byer, "Second-harmonic generation of green light in periodically poled planar lithium niobate waveguide," Electronics Letters **25** (3), 174-5 (1989).

13 J. Webjorn, F. Laurell, and G. Arvidsson, "Fabrication of periodically domain-inverted channel waveguides in lithium niobate for second harmonic generation," Journal of Lightwave Technology **7** (10), 1597-600 (1989).

14 M. Yamada, N. Nada, M. Saitoh *et al*., "First-order quasi-phased matched $LiNbO_3$ waveguide periodically poled by applying an external field for efficient blue second-harmonic generation," Applied Physics Letters **62** (5), 435-6 (1993).

15 R. L. Byer, "Quasi-phase matched nonlinear materials and application to devices," Nonlinear Optics, Principles, Materials, Phenomena and Devices **7** (3-4), 235-45 (1994).

16 R. L. Byer, "Quasi-phase matched nonlinear interactions and devices," Journal of Nonlinear Optical Physics & Materials **6** (4), 549-591 (1997).

17 L. E. Myers, G. D. Miller, R. C. Eckardt *et al*., "Quasi-phase-matched 1.064-µm-pumped optical parametric oscillator in bulk periodically poled $LiNbO_3$," Optics Letters **20** (1), 52-4 (1995).

18 L. E. Myers, W. R. Bosenberg, J. I. Alexander *et al*., "CW singly-resonant optical parametric oscillators based on 1.064-µm-pumped periodically poled $LiNbO_3$," in *OSA Trends in Optics and Photonics on Advanced Solid State Lasers. Vol.1. From the Topical Meeting*, edited by S. A. Payne and C. R. Pollock (Opt. Soc. America, Washington, DC, USA, 1996), pp. 35-7.

19 V. Pruneri, R. Koch, P. G. Kazansky *et al*., "49 mW of CW blue light generated by first-order quasi-phase-matched frequency doubling of a diode-pumped 946-nm Nd:YAG laser," Optics Letters **20** (23), 2375-7 (1995).

20 G. D. Miller, R. G. Batchko, W. M. Tulloch *et al*., "42%-efficient single-pass CW second-harmonic generation in periodically poled lithium niobate," Optics Letters **22** (24), 1834-6 (1997).

CHAPTER 2. MODELING DOMAIN KINETICS DURING ELECTRIC FIELD PERIODIC POLING

In the "early" days of $LiNbO_3$ electric field periodic poling (1991 to 1994), the list of parameters that influenced the quality of a domain pattern seemed unmanageably large. Anecdotes drifted into our laboratory from one month to the next telling of the benefits of one metal over another, the need for vacuum, or oil, or photoresist as an insulator, and even the importance of choosing the correct polarity power supply. It became increasingly important to have a systematic approach to the development of poling recipes, an approach based on measurable material properties and the ability to model the poling process. Modeling represented a radical departure from other recipe development efforts at the time since it provided for parameter optimization without requiring time-consuming iterative experiments. In many ways the model developed during the course of this research was pragmatic in its focus. Rather than striving to produce a general model of the ferroelectric properties of $LiNbO_3$, the effort was directed toward identifying and optimizing those parameters contributing most significantly to repeatable, good-quality periodic domain patterns in $LiNbO_3$.

The model presented in this chapter consists of a descriptive part and a computational part. In the descriptive part, domain kinetics are described with an emphasis on simplifying assumptions based on experimental observations. These assumptions provide the basis for the computational part of the model. The descriptive part of the model also provides a basis for choosing electrode and insulating materials, for identifying important factors in fabrication, for the design of poling waveforms, and a means for interpreting poling results. The computational part of the model allows the effects of parameters such as electrode duty cycle, insulator type and thickness, poling waveform, and sample thickness to be studied and optimized before beginning the design of a photolithography mask or performing a poling experiment.

This chapter is divided into four sections. The first section presents the descriptive part of the model of domain kinetics during electric field periodic poling. The second

section combines experimental data presented in the first section with the electrostatics of periodic poling to form the computational part of the model of electric field periodic poling. The third section presents a recipe for fabricating 0.5-mm-thick 75-mm-diameter wafers of 6.5-μm-period electric field periodically poled $LiNbO_3$ where the materials, electrode dimensions, and poling waveform were based on the model. The final section is a summary of the chapter.

2.1. Descriptive model of domain kinetics during electric field periodic poling

To generate a model of domain kinetics during electric field periodic poling, it was important to identify a set of simplifying assumptions that permitted us to interpret experimental results and to refine our fabrication techniques. These assumptions provided us with a simple model of poling, where factors of secondary significance were not directly included. However, by understanding the limitations of each assumption, the interplay of secondary factors could be identified and managed. The assumptions and the analysis upon which they are based are presented first, followed by a presentation of the descriptive part of the model.

2.1.1. Assumptions

The first published images[1] of *y*-face cross-sections of electric field periodically poled $LiNbO_3$, along with those that followed in subsequent publications,[2-6] raised a number of questions about the physics of the poling process. As can be seen in the drawing shown in Figure 2.1, the domain walls were often quite straight and parallel to the crystal *z*-axis, from the electroded surface into the bulk of the crystal. It was not obvious why this should be the case, especially in the vicinity of the electrodes where the electric field was highly non-uniform. Similar behavior can also been seen in $LiTaO_3$[7-10]. The domains had a greater width than the electrodes, indicating that spontaneous polarization charge was deposited on the surface of the ferroelectric between the electrodes. In the absence of conduction this charge would be unscreened, and would give rise to fields of the sign *opposite* to that required for domain reversal (see Appendix A).

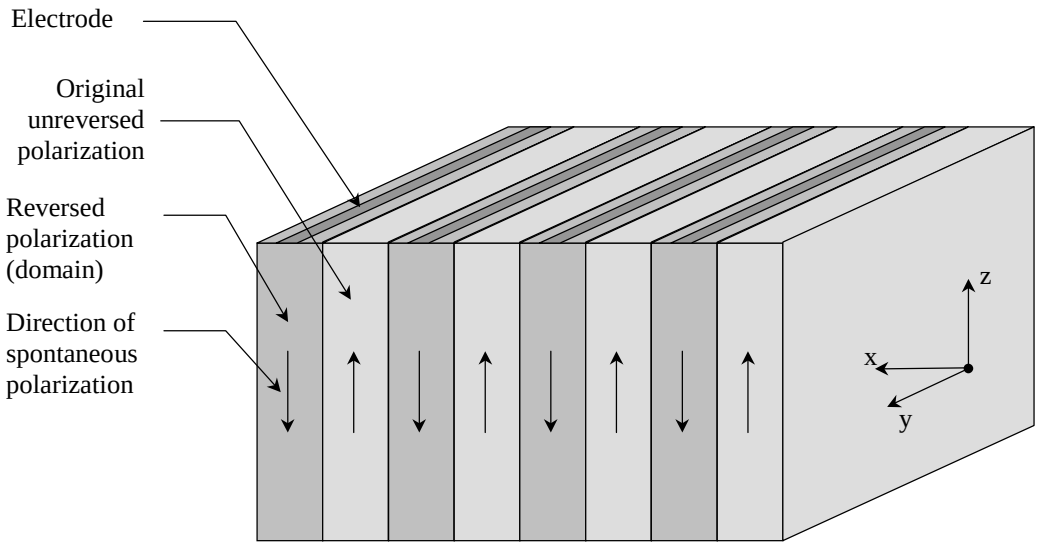

Figure 2.1. Diagram of typical domain configuration shown in published cross-section photomicrographs of electric field periodically poled $LiNbO_3$.

One possible explanation for this behavior is that partial screening occurs, allowing the local fields to remain large enough to permit reversal of the spontaneous polarization near the ferroelectric-insulator interface between the electrodes. However, poling is typically performed at fields where the growth rate of domains is a strong function of the applied field (see Section 2.1.2.5.); unless screening is nearly complete, the fields near the ferroelectric-insulator interface between the electrodes would not be expected to sustain domain growth. Significant screening would result in domains whose growth is at best loosely correlated with the electrode structure.

A second possible explanation is that the electric field near the ferroelectric-insulator interface can be reduced by re-distribution of charge away from the interface. Nonlinear conductivity was considered as a potential mechanism here. However, two difficulties arise: First, the electric field is largest in the vicinity of the electrode edge and would result in charge injection and partial screening even while spontaneous polarization charge is being distributed away from the ferroelectric-insulator interface. Second, the sensitivity of domain growth to the applied field would prevent domain growth all the way to the ferroelectric-insulator interface.

Rather than investigating further these and other potential explanations, we observed simply that localized fields appear to have at best a minor influence on the shape of

domain walls in $LiNbO_3$. We also observed that domain walls are generally straight and parallel to the crystal *y*-axis. Therefore, the first simplifying assumption used in the model is that domain walls are flat and normal to the crystal *x*-axis, even when there is no screening or re-distribution of charge at the ferroelectric-insulator interface.

That a domain can continue to grow when a portion near the surface is in a strong field opposing domain growth suggests that, rather than the local poling field, the poling field averaged over some portion of the domain wall dominates its behavior. For laminar domains whose width in the *x*-direction is small compared to the thickness of the ferroelectric, and where the electric field varies only in the *x*-*z* plane, this observation leads to the second simplifying assumption used in the model: Domain wall motion is governed by the *z*-component of the electric field averaged over the *x*-*z* cross-sectional area of the domain.

Another observation from published poling results is that the domains were of fairly uniform width. Since all of the domains were grown with approximately the same field for the same time, this observation suggests that domain wall velocity as a function of applied field is fairly uniform throughout the volume of the crystal. This leads to the third simplifying assumption that the functional relationship between domain wall velocity and the *z*-component of the electric field averaged over the *x*-*z* cross-sectional area of the domain is the same everywhere in the crystal.

Typically, domains in electric field periodically poled $LiNbO_3$ are approximately centered under their electrodes, indicating that domain nucleation sites are strongly correlated with the electrodes themselves. In addition to the nucleation sites associated with the electrodes, the crystal itself has intrinsic nucleation sites, as shown in Figure 2.2. Although these nucleation sites cause domain pattern defects, their effects can be minimized by choosing optimum poling conditions and through careful sample preparation. The fourth simplifying assumption of the model is that nucleation occurs exclusively at the electrodes.

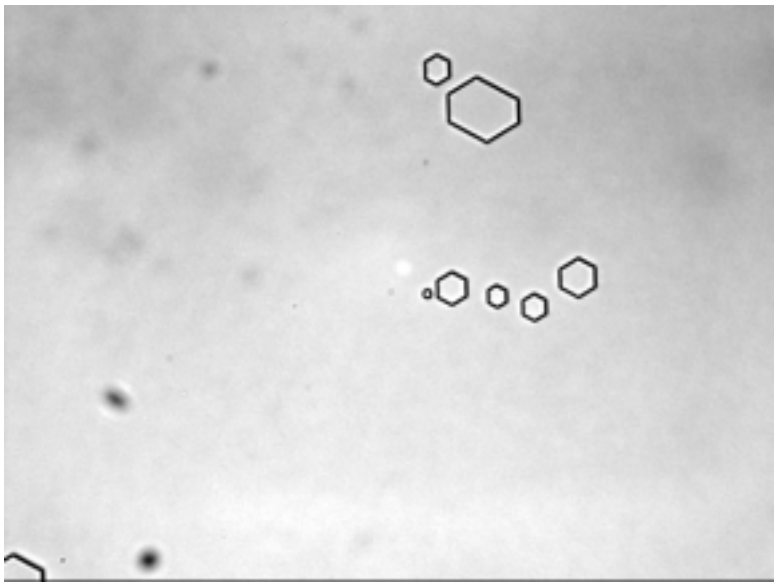

Figure 2.2. Image of domains on the +*z* face of $LiNbO_3$ after poling for 10 s at 21 kV/mm and etching in hydrofluoric acid for 5 min. The viewing field is 100-µm wide and 75-µm tall.

In all published cases, the surface of the $LiNbO_3$ samples between the electrodes was insulated, whether by vacuum, oil, or a dielectric coating. It was apparent that screening of the spontaneous polarization charge deposited between the electrodes as a result of domain wall motion out from under the electrode edges was to be avoided. Consequently, the fifth simplifying assumption of the model is that there is no bulk or surface conductivity. More precisely, the dielectric relaxation times of the ferroelectric and insulator are assumed to be much longer than the poling time.

Summarizing, the assumptions used in the development of the model of domain kinetics during electric field periodic poling are:

1. Domain walls are flat and normal to the crystal *x*-axis.
2. Domain wall motion is governed by the *z*-component of the electric field averaged over the *x*-*z* cross-section of the domain.
3. The functional relationship between domain wall velocity and the *z*-component of the electric field averaged over the *x*-*z* cross-section of the domain is the same everywhere in the crystal.
4. Nucleation occurs exclusively at the electrodes.
5. The dielectric relaxation times of the ferroelectric and insulator are assumed to be much longer than the poling time.

2.1.2. Description of domain kinetics during electric field periodic poling

With these assumptions, domain kinetics during electric field periodic poling are given in six stages as shown in Figure 2.3. After describing the sample preparation techniques used to study these stages, a discussion of each stage follows, where the behavior of $LiNbO_3$ with both uniform and periodic electrodes is analyzed.

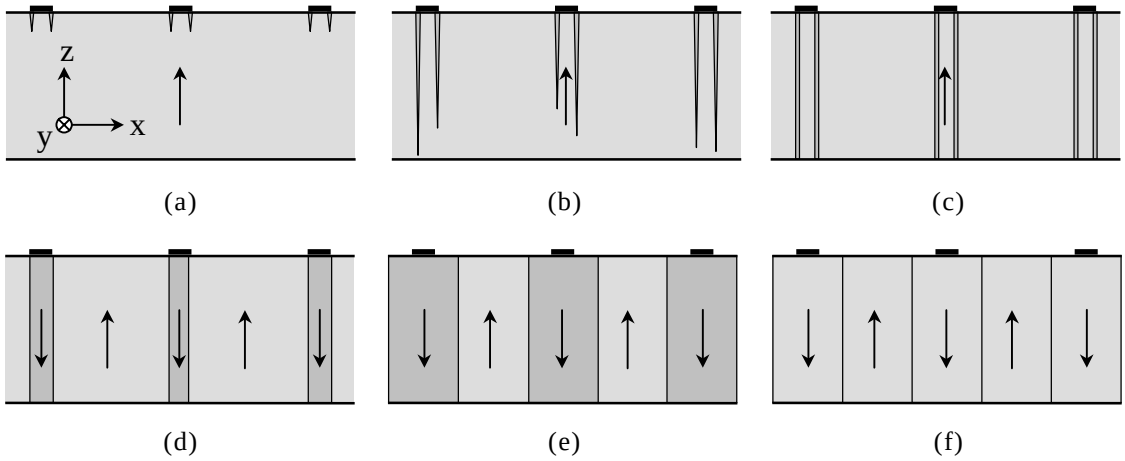

Figure 2.3. The six stages of domain kinetics during electric field periodic poling. (a) Domain nucleation at the electrode edges. (b) Domain tip propagation toward the opposite face of the crystal. (c) Termination of the tip at the opposite side of the crystal. (d) Rapid coalescence under the electrodes. (e) Propagation of the domain walls out from under the electrodes. (f) Stabilization of the new domains.

In the experimental study of the stages of domain kinetics, uniformly electroded samples were prepared with uniform electrolyte contacts. The contacts were applied to the polar faces of 6.0-mm-square single-domain samples with thickness' ranging from 250 µm to 1 mm. The samples were clamped between o-rings in a fixture of the type described in Ref. [11]. Electrolyte solutions were chosen because metallic contacts resulted in observations highly dependent on the choice of metal and its method of application; experimental outcomes were not dependent on the choice of electrolyte. Among the electrolytes tested were various concentrations of lithium chloride or sodium chloride in deionized water, pure deionized water, tap water, isopropanol, and methanol.

Samples prepared with periodic electrodes had lithographically defined structures with periods from 1.75 µm to 15 µm. The metal was one of aluminum, titanium, tantalum, chrome, nickel, or nichrome. Both evaporation and sputtering were studied for their effect. In cases where the electrode pattern was defined using lift-off, the electrode

pattern was over-coated with photoresist or spin-on-glass, or poling was performed in dielectric oil. In other cases, samples were prepared with metal deposited over patterned photoresist, contacting the $LiNbO_3$ surface through the patterned openings. Samples were also clamped between o-rings as in the case of uniformly electroded samples and contacted using electrolyte. In the case where the electrode pattern was over-coated with an insulator, an opening in the insulator was provided to allow the electrolyte to make contact.

Anti-polar electric fields (electric fields whose direction is opposite to that of the spontaneous polarization) ranging in magnitude from 19 kV/mm to 60 kV/mm were applied for with pulse lengths ranging from 100 ns to 3 h. A Trek Model 20/20 high voltage amplifier was used for pulses 10 µs and longer, and a Hughes Crossatron 45 kV switch was used for shorter pulses. After poling pulses were applied, domains were revealed on samples using hydrofluoric acid at room temperature for 5 min. Use of this observation technique is permissible only if the domain size remains unchanged after the poling pulse terminates. The poling pulses were designed to allow the domains to stabilize without further growth.

2.1.2.1. Nucleation

The first stage in domain formation is nucleation. It appears that each individual domain has a single starting point, called the nucleation site. Nucleation sites are typically located on both sample faces. Nucleation sites do not appear to be Poisson distributed; they tend to be grouped in clusters, in arcing or linear paths, or near domains already in the wall propagation stage. Nucleation site density (NSD) is field- and time-dependent for fields below 21 kV/mm. For fields from 24 kV/mm to 64 kV/mm and pulse durations down to 100 ns (the limitations of our test equipment), NSD was independent of field strength and pulse width. The maximum NSD observed using LiCl electrolyte contacts was on the order of 1000 nuclei/mm^2.

Samples were tested with 3.0 mm diameter metal dots deposited on their $+z$ or $-z$ faces. The electrolyte contact diameter was 4.25 mm, making it possible to compare treated and untreated areas on the same sample. Evaporated aluminum and sputtered titanium, chrome, molybdenum, and nickel were tested. Each metal exhibited a

noticeable effect on NSD, in some cases suppressing nucleation, and in others enhancing it. In particular, sputtered chrome and nickel each greatly increased NSD when applied to the +*z* face. Figure 2.4 shows a view of a sample poled with a 3-mm-diameter spot of 100Å-thick sputtered nickel on the +*z* face taken with crossed polarizers through the –*z* face. The figure shows the large difference in NSD between the metallized and un-metallized areas.

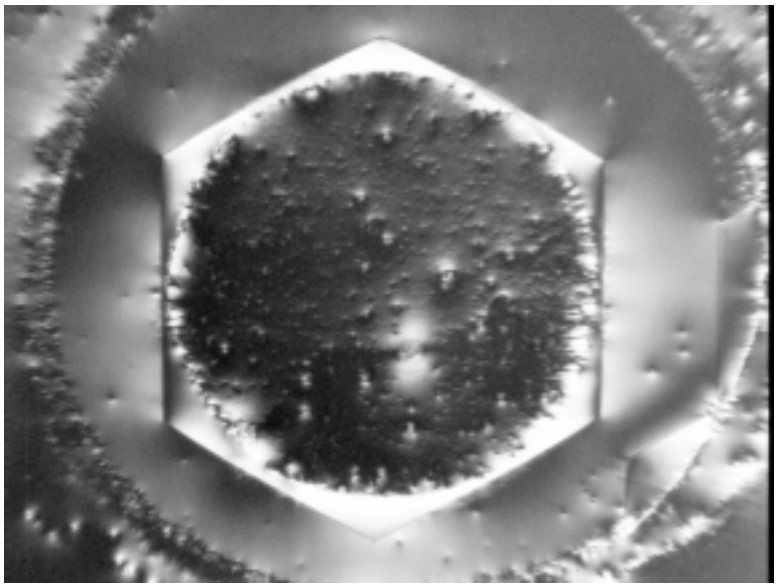

Figure 2.4. Crossed-polarized image of sample poled with a 3-mm-diameter spot of 100Å-thick sputtered nickel on the +*z* face. The view is taken through the –*z* face. The large hexagon is reversed material. The bright spots are nucleation sites. Note the large difference in NSD between the metallized and un-metallized areas.

Most recently, sputtered nichrome was tested on the +*z* face and was found to provide an even larger NSD than sputtered chrome or nickel. Table 2.1 shows the relative influence of each contact material on NSD based on qualitative observations. Note that the electrolyte solution LiCl:H_2O is used as the reference contacting material; we found that NSD was the same for both faces using this electrolyte. A systematic and quantitative investigation of the influence of electrode materials on NSD would be useful for increasing our understanding of the nucleation process and for future improvements to electric field periodic poling.

Electrode material	+z face	-z face
Electrolyte ($LiCl:H_2O$)	0	0
Evaporated aluminum	+1	-5
Sputtered titanium	0	-1
Sputtered molybdenum	-1	+2
Sputtered chrome	+5	-2
Sputtered nickel	+7	-2
Sputtered nichrome	+10	N/A

Table 2.1. Relative influence on NSD for various electrode materials. Numbers from +10 to – 10 are used to indicate approximate order between the materials.

Periodic electrodes caused a significant increase in NSD compared to uniform electrolyte contacts. The domains nucleated along the edges of the electrodes with a linear density of 0.1– 2 nuclei/µm. Assuming an electrode period of 10 µm and a linear density of 1 nucleus/µm, the NSD is 200,000 nuclei/mm^2, compared with 1000 nuclei/mm^2 for plain $LiNbO_3$. The electrode/insulator configuration and the choice of electrode material strongly influence NSD; the highest values of NSD were observed when using sputtered nichrome stripes over-coated with spin-on-glass.

2.1.2.2. Tip propagation

A domain nucleus in lithium niobate can be represented as a six-walled pyramid, with a hexagonal base at the surface of the crystal, and its apex, or tip, close to but just below the surface. The tip propagates parallel to the polar axis to the opposite face of the crystal, dominating the growth of the domain in this stage. As the tip propagates, the diameter of the base increases. The ratio of tip velocity to the wall velocity at the base is between 100:1 and 1000:1, as deduced from short-pulse poling experiments where domains on both the +*z* face and –*z* face were mapped to find domains that had not propagated through the crystal. Assuming that the greatest tip velocity of these non-through domains would place their tips just below the crystal surface, the velocity ratio was computed by dividing the crystal thickness by one-half the diameter of the base of

the domain. Further investigation is required to determine the relationship between tip velocity and applied field and to understand the shape of the domain in this stage.

During tip propagation, domain tips from adjacent electrodes can merge, leading to the formation of a single large domain instead of two. The merging of domains reduces the effective nonlinearity of PPLN and occurs mainly during the tip propagation stage. One source of domain merging is substrate inhomogeneity, which causes domain tips to wander from a strictly *z*-directed path. While the exact nature of this inhomogeneity is not yet known, its presence can be observed by applying short poling pulses to samples uniformly contacted by electrolyte so as to form domains approximately 10 µm in diameter. After etching, clusters and long strands of domains can often be found, with no apparent cause for the behavior attributable to surface conditions (e.g. scratches). The distribution of nuclei does not appear Poissonian, and is suggestive of spatial variations in some property of the ferroelectric crystal. Microscopic examination of these clusters often reveals multiple distinct domains on one face of the crystal, and a single, larger domain directly opposite them on the other crystal face, suggesting that the tips of the individual domains merged during tip propagation. Also, the pattern of a domain cluster on one face often appears distorted when compared to its complement on the opposite face, suggesting that the tips deviated from a strictly *z*-directed path. For additional information on the effect of inhomogeneities in the ferroelectric on domain formation, see Reference 12.

Another important source of domain merging is tip-to-tip interactions. When two domain tips are in close proximity, the unscreened polarization charge on their walls slightly increases the electric field in the region between them.[13] This increased field leads to an increased growth rate on the walls closest to the nearby domain. The increased growth rate causes the paths of the domain tips to merge. In electric field periodic poling, this type of merging is preferred between closely spaced tips generated by the same electrode stripe. However, under conditions of low NSD where the closest tips are those generated by separate electrode stripes, merging results in the loss of a domain and reduction of the effective nonlinearity. Examples of domain merging can be seen in Figure 2.5. The sample shown in this figure had periodic openings in 0.5-µm-thick spin-on-glass on the +*z*-face. The openings were 1-µm wide and were

spaced on a 6.5-µm period. No metal was placed in contact with the surface of the $LiNbO_3$.

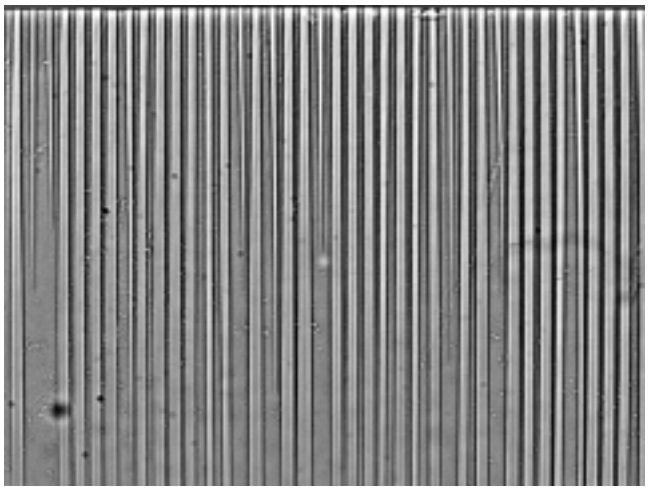

Figure 2.5. 6.5 µm domain period in 500 µm thick $LiNbO_3$ showing domain merging. The view is of the former +*y*-face near the former +*z*-face. Dark bands are domain-reversed. The sample was poled at 20.75 kV/mm with a 6.5-µm electrode period using 1-µm-wide electrolyte contact openings in a 0.5-µm-thick spin-on-glass insulator.

While the +*z* faces of samples prepared for nucleation studies show linear arrays of domains along the electrode edges, the –*z* faces of those samples often show single continuous lines; the domain tips merged before reaching the –*z* face. For electrode periods >15 µm, merging happens almost exclusively under the electrodes, depending on the field used during poling. Below 10 µm, the frequency with which domains from adjacent electrodes merge increases rapidly. The depth at which domains from adjacent electrodes merge is ~100 µm[5].

2.1.2.3. Tip termination

When the tips of isolated domains contact the opposite face of the crystal, the walls of the domain straighten on a time scale shorter than 1 µs, creating a hexagonal shape with the same diameter as that of the original nucleus. This time scale was determined during the tip velocity experiments: The same samples that produced domains that had not propagated completely from one crystal face to the other also produced domains that did propagate through, and the smallest of both types of domain had approximately the same diameter. Since the pulse widths used during these experiments were shorter than 1 µs,

the conclusion drawn was that the transition from the tip propagation to the tip termination regime was less than 1 µs. During this brief stage, the domain greatly reduces its electrostatic interaction with neighboring domains as a result of its walls becoming parallel to the *z* axis. When a pair of domain tips merge as they propagate through the crystal, the termination event results in a larger domain than would occur in the absence of merging, due to the large energy penalty associated with tilted domain walls. The close proximity of domain tips generated by a single stripe electrode gives rise to merging under the electrode, and the tip termination stage contributes to complete domain reversal under the electrode.

2.1.2.4. Rapid coalescence

Adjacent domains rapidly coalesce to form a larger domain when their walls touch. In Figure 2.6 below, a sequence of four poling pulses was applied to a 0.5-mm-thick sample of $LiNbO_3$, with a two-minute etch in fresh hydrofluoric acid at room temperature after each pulse. The pulses were 20.75 kV/mm for 800 ms, 24.3 kV/mm for 2.5 µs, 28.2 kV/mm for 2.8 µs, and 31.55 kV/mm for 0.4 µs. Note that at the third pulse, a second domain nucleated within several microns of the first. During the fourth pulse, the domain walls of the two domains rapidly merged, forming a single larger domain.

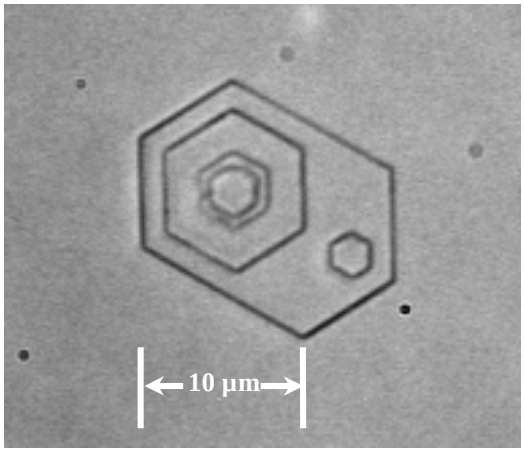

Figure 2.6. Sequence of poling-etching events where a uniformly electroded sample of $LiNbO_3$ was given a series of short poling pulses, each followed by etching for two minutes in hydrofluoric acid. The +*z*-face of the sample is shown.

The velocity of the domain wall in the region where the two domains made contact was many times larger than the domain wall velocity elsewhere. Several researchers have noted the similarity between this behavior and that often seen during faceted crystal growth,[14,15] and its origin warrants further investigation.

Samples with periodic electrodes benefit from rapid coalescence, since it provides a means for domains to fill in the space under the electrodes before they begin to spread outward. An example of this behavior can be seen in Figure 2.7. This sample had a 13.25 µm period pattern of 1.25-µm-wide sputtered nickel electrodes, overcoated with hard-baked photoresist. The sample was 0.25-mm thick and was poled at 20.25 kV/mm for 7.7 ms. Region A shows signs of nucleation along the electrode edges, most frequently along the right edge of the electrodes in this photo. In region B, domains coalescence began under the electrodes. In region C, coalescence is complete. Finally, in region D, the domains began to spread out from beneath the electrodes.

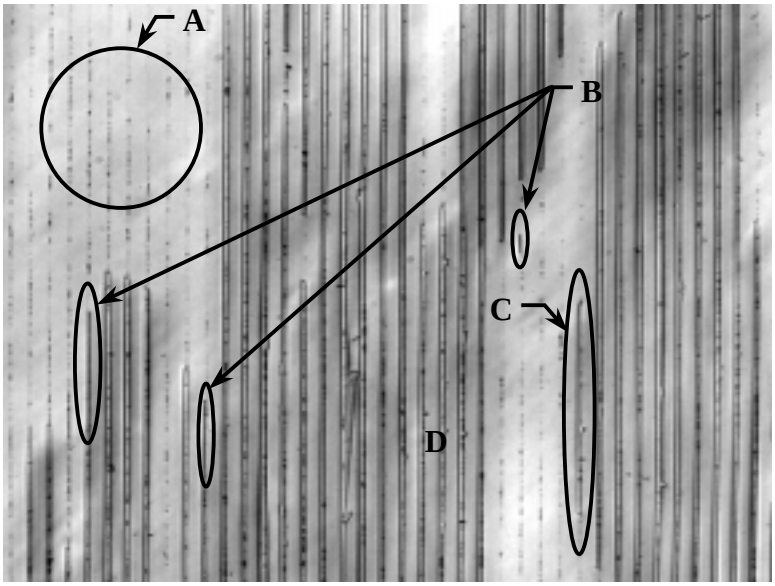

Figure 2.7. Stages of domain formation for 0.25-mm-thick $LiNbO_3$ sample with 13.25-µm-period sputtered nickel electrodes, 1.25-µm wide. The electrodes were overcoated with 0.25-µm-thick hard-baked photoresist. The sample was poled for 7.7 ms at 20.25 kV/mm. The etched +*z* face shows nucleation primarily along the electrode edges in Region A, partial coalescence under the electrodes in Region B, complete coalescence under the electrodes in Region C, and spreading of the domains beyond the electrodes in Region D.

While the sample shown in Figure 2.7 does not comply with the assumptions of the simple model, a great deal can be learned by studying the ways in which it deviates from

those assumptions. Implicit in the assumptions is uniformity and simultaneity. The low density of nucleation sites and their non-uniform distribution can be expected to contribute to poor domain pattern quality. Rather than coalescence occurring simultaneously at a large number of sites along each electrode, coalescence occurs on the *y* face of domains growing along the electrodes. As each domain grows along its electrode, it spreads out from under the electrode at the site where coalescence first began, resulting in poor domain duty cycle uniformity. Close examination of the image shows that nucleation site density is typically largest on the right side of the electrodes, pointing to a potential problem in the lift-off process. Finally, in the center of the image, a domain wall is seen to have spread badly beyond the edge of the electrode. This behavior suggests that there may have been some conduction between the photoresist and the surface of the $LiNbO_3$, permitting the spontaneous polarization charge to be partially screened. Conduction can be caused by adhesion problems typically associated with inadequate preparation of the $LiNbO_3$ surface.

2.1.2.5. Wall propagation

When the tip of an isolated domain terminates at the opposite face of a sample, the diameter of the domain at both faces rapidly equalizes. The domain has a hexagonal cross-section in the plane normal to the polar axis as shown in Figure 2.2, and its facets propagate in the direction of the crystal *a* axis with equal velocity. By obtaining the relationship between domain wall velocity and electric field for samples with uniform electrodes, domain kinetics during the wall propagation phase of electric field periodic poling can be calculated. In addition, the relationship can be studied to identify whether there is a field at which domain wall velocity is most sensitive to changes in the field.

Domain wall velocity was studied using the method of Miller and Savage[16], where a poling pulse is applied to a sample for a time T, the sample is etched, the radius R of the largest domain is measured, and the velocity is taken as R/T. The reason for taking the largest domain is that it represents the one that nucleated soonest after the beginning of the poling pulse. The radius of smaller domains was also noted to get a sense for the time-dependence of nucleation for different fields. Care had to be taken in the design of the waveform and poling apparatus to allow domains to stabilize; newly formed domains

are unstable and require continued application of field until they relax. Stabilization is discussed in more detail in the next section.

Figure 2.8 shows domain wall velocity data for fields between 19 and 28 kV/mm, with domain wall velocity varying over 10 orders of magnitude in this interval.

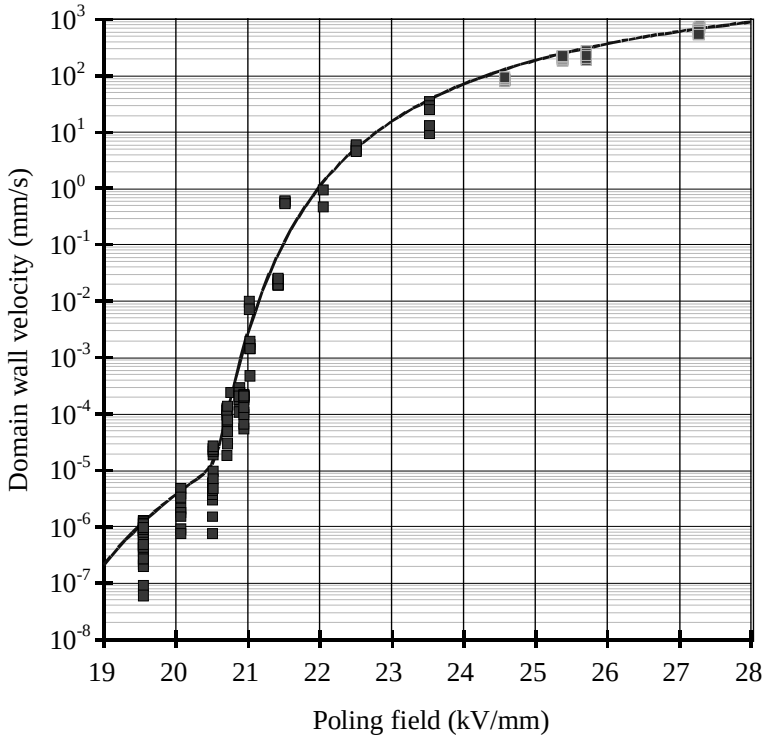

Figure 2.8 Domain wall velocity versus poling field. The squares are experimental data and the solid curve is the fit based on the equation discussed below.

The scatter in data points at fields below 21 kV/mm shows that some domains nucleate before others, indicating that nucleation is a time-dependent process at low fields; the longer the field is applied, the greater the number of nucleation sites. The relative lack of scatter above 21 kV/mm shows that nucleation occurs on a time scale much shorter than the pulse duration with increasing field and that the number of nuclei-per-unit-area does not increase with increased pulse length in this regime. To investigate this behavior further, samples were poled at fields up to 64 kV/mm with no noticeable increase in nucleation site density, and all the domains on each sample were nearly equal in size. (It is interesting to note that, at fields above ~30 kV/mm, the domains took on a triangular shape.) The implication of this finding is significant because it implies that there are a

finite number of nucleation sites available in $LiNbO_3$. Previous models[17] indicate that nucleation rate is proportional to $\exp(-\Delta W/kT)$, where ΔW is the energy associated with domain nucleation, k is Boltzmann's constant, and T is temperature. This measurement suggests that all available nucleation sites are activated at the beginning of the poling pulse for fields above 24 kV/mm.

In $BaTiO_3$, domain wall velocity data was described well by a fitting function of the form[16]

$$v(E) = v_\infty \exp(-\delta/E). \tag{2.1}$$

This function however cannot fit the apparent inflection in the data that occurs around 20.5 kV/mm. The data appeared to be generated by a superposition of two functions similar to Equation (2.1), differing in that each function's domain wall velocity goes to zero for some positive non-zero value of electric field. Thus, the fitting function applied to this data is

$$v(E) = \Phi(E - E_1)\, v_1 \exp\left(-\frac{\delta_1 E_1}{E - E_1}\right) + \Phi(E - E_2)\, v_2 \exp\left(-\frac{\delta_2 E_2}{E - E_2}\right) \tag{2.2}$$

where Φ is the Heaviside step function and the fitting parameters are given in Table 2.2.

$E_1 = 19.4$ kV/mm	$E_2 = 15.0$ kV/mm
$v_1 = 16.3$ m/sec	$v_2 = 362$ μm/sec
$\delta_1 = 1.29$	$\delta_2 = 3.83$

Table 2.2. Fitting parameters for velocity-field function.

Equation (2.2) can be used to determine the field at which domain wall velocity is most sensitive to changes in the average field in the crystal. As domains spread out from under the electrodes, the unscreened spontaneous polarization charge deposited on the surface of the crystal lowers the average field seen by the domain, slowing its growth. By periodic poling with the field at which domain wall velocity is most sensitive to changes in the average field, a strong negative feedback mechanism is created, preventing the excessive spreading of domains beyond the electrodes. This optimum field can be determined from the peak of the derivative of the logarithm of Equation (2.2), also referred to as the contrast curve. Figure 2.9 shows the contrast curve for the velocity-field function. The curve shows that the domain wall velocity is most sensitive to slight

variations in the applied field at 20.75 kV/mm, varying 5.5 orders of magnitude per kV/mm at that field.

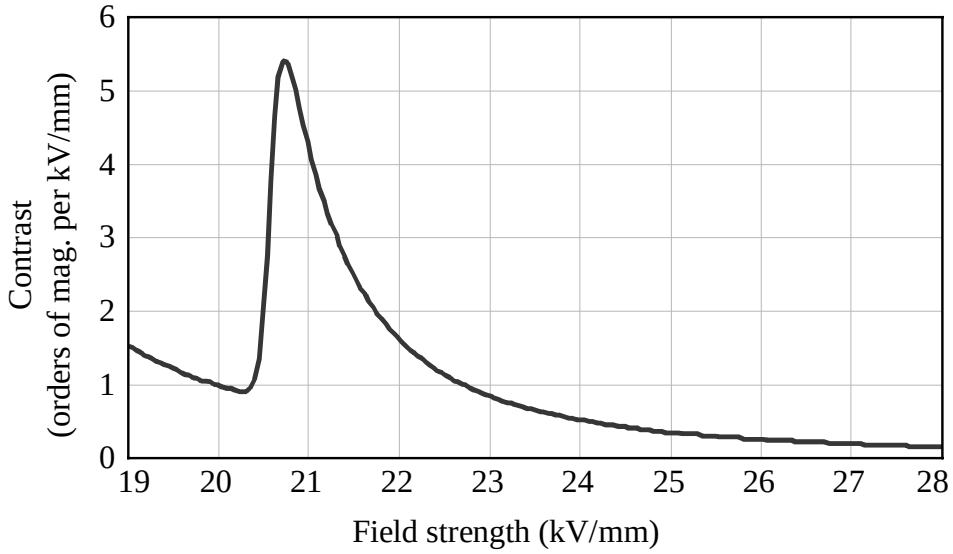

Figure 2.9. Contrast curve (derivative of the log of domain wall velocity versus poling field) for $LiNbO_3$. The curve shows that the optimum poling field is 20.75 kV/mm.

2.1.2.6. Stabilization

Newly formed domains exhibit a time-dependent coercive field. This field is initially ~ -17.5 kV/mm and decays in ~60 ms to 0 kV/mm. A positive value of the coercive field indicates that the applied field opposes the direction of the spontaneous polarization, which is the usual situation in ferroelectrics. A negative value indicates that the direction of the applied field causing domain reversal is the *same* as that of the spontaneous polarization. In the case of newly formed domains, a field in the same direction as the spontaneous polarization with a magnitude of 17.5 kV/mm or more is required to maintain domain orientation. Reducing the externally applied field to 0 kV/mm in less than 60 ms will cause domains to flip back in a process called 'backswitching'[18]. Within one day of domain reversal, the coercive field approaches ~+19 kV/mm, and remains unchanged even after several days at room temperature. Myers[19] reported that heating for 1 h at 120°C restores the coercive field to its original value, 21 kV/mm. He also observed that domains remain stable at temperatures at least as high as 800°C.

Chao *et al.*[20] reported a similar time-dependence of the coercive field for $LiTaO_3$ and showed that illumination increased the rate of recovery. In this and other reports[21-23], a time-varying built-in space-charge field was hypothesized as the cause of this behavior, using the electro-optic effect and the attraction of charged particles in support of the hypothesis. Recently, this hypothesis has been applied to $LiNbO_3$[24]. In these reports, asymmetry of the hysteresis loop is used as an indicator of the possibility of a built-in field. However, an alternative hypothesis must be considered – that the asymmetry may be attributed to a change in coercivity associated with the poling event. An example of a hysteresis loop in $LiNbO_3$ is shown in Figure 2.10, indicating that the coercive field for reversing the original polarization is 22.9 kV/mm, while the coercive field for restoring the original polarization is 17.6 kV/mm. This hysteresis loop was obtained using a poling waveform like that shown in Figure 2.11, with the exception that the time between poling events was 5 minutes.

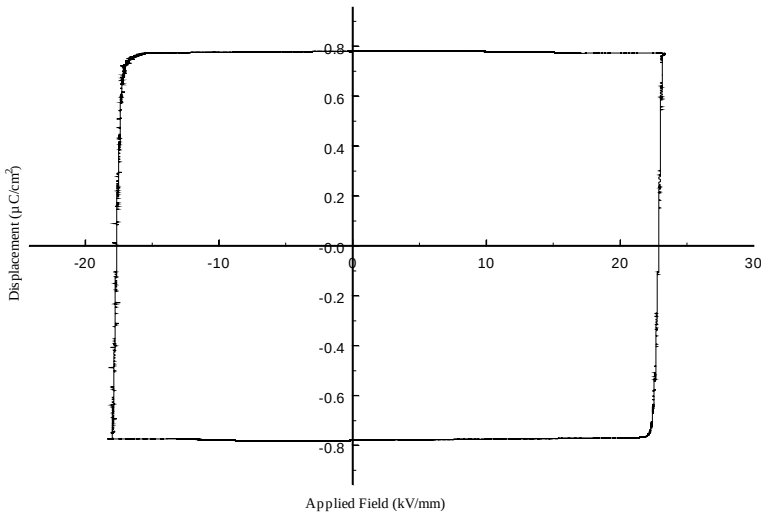

Figure 2.10. Hysteresis loop for $LiNbO_3$, showing that the coercive field for reversing the original polarization is 22.9 kV/mm, and that the coercive field for restoring the original polarization is 17.6 kV/mm. The time between poling events was 5 min. This hysteresis loop is the first recorded in $LiNbO_3$[25].

To determine conclusively the presence of a time-varying built-in field, the change in charge delivered to the crystal surfaces should be measured as the field changes. This measurement is difficult due to the fact that it represents a very small fraction of the total current. A 17.5 kV/mm change in 60 ms on a typical sample with a poled diameter of

4.25 mm results in a relaxation current of 1 μA, or 0.02% of the usual 5 mA poling current. Furthermore, poling must be completed in less time than that required for relaxation of the built-in field, otherwise the relaxation current cannot be separated from the poling current. We report here the first direct evidence of a built-in electric field that changes sign as a result of poling. This evidence was obtained from an analysis of poling waveforms obtained from hysteresis measurements.

During the generation of hysteresis loops, it is important that poling comes to completion before the applied field begins to decrease. After poling is complete, the current delivered to the sample should stop, with the possible exception of leakage current in the poling fixture. It is possible to ascertain from the poling waveform whether leakage is a significant contributor to the current waveform by analyzing the proportionality between the voltage and current waveforms. Another source of current is displacement current associated with the changes in voltage across the sample. Finally, electrical noise and discretization errors contribute to the current waveform. Fortunately, electrical noise of sufficient amplitude coupled with a sufficiently high sampling rate can be used to digitally remove discretization errors. In these experiments a Lecroy 9304M digital sampling oscilloscope was used, and the waveforms were saved for later processing.

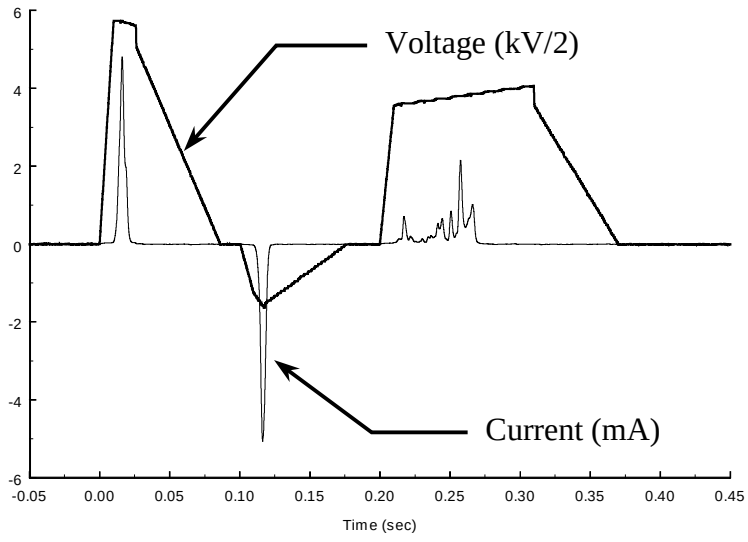

Figure 2.11. Voltage and current waveforms for hysteresis loop measurements.

Figure 2.11 shows a voltage waveform used in a hysteresis loop measurement with its accompanying current trace. The current trace was smoothed using a 333 Hz real gaussian low-pass filter to suppress discretization noise. By expanding the vertical scale to reveal the details of the current waveform as shown in Figure 2.12, a positive 4.2-ms-long current pulse can be seen shortly after the poling field is reduced. The pulse is of the opposite sign of the displacement current. Leakage current is significantly less than the displacement current. The charge delivered in this pulse, 35 nC, is consistent with a change in the internal field of 9.6 kV/mm. This behavior was also found in other poling waveforms where poling was completed in 10 ms or less.

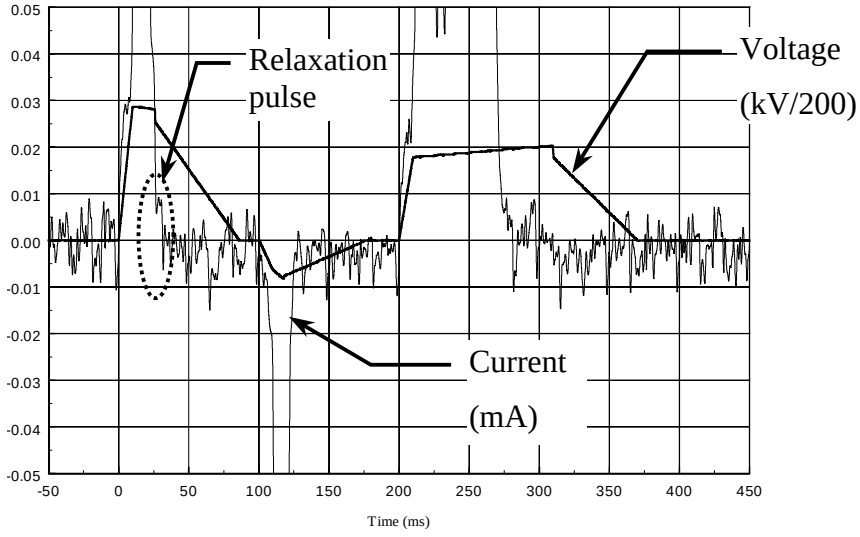

Figure 2.12. Stabilization current taken from zoom-in of region outlined in Figure 2.11. The voltage waveform is re-scaled to show the presence of a positive current pulse after the poling field was reduced. This pulse is caused by the relaxation of an electric field internal to the crystal.

In electric field periodic poling, the poling waveform should be designed to ramp from the poling voltage to zero in 60 ms or longer to suppress backswitching. However, the electrostatics of periodic poling (discussed in detail in Appendix A) gives rise to the possibility that some backswitching in the vicinity of the electrode edges may be difficult to avoid. The lack of screening on the $LiNbO_3$ surface between the electrodes results in anti-polar fields that are increased due to relaxation of the built-in field. These anti-polar

fields can nucleate backswitching at the electrode edges. Evidence of small backswitched domains can be seen along the electrode edges in Region D of Figure 2.7.

2.2. Computational model of domain kinetics during electric field periodic poling

In Section 2.1.2.5, we described a negative feedback mechanism that slows domain walls as they spread out from under the electrodes. In this Section, we show that this mechanism can be simulated using the model's assumptions, the electrostatics calculations presented in Appendix A, and Equation (2.2), which is also referred to as the velocity-field equation.

In electric field periodic poling, the main objective is to obtain a specified domain period and duty cycle with acceptable uniformity throughout the volume of the crystal. While the domain period is assured by the lithography that produces the electrode patterns, many factors influence duty cycle uniformity. Good duty cycle uniformity is important because it contributes to the efficiency of QPM devices[26] and, in the case of photorefractives like $LiNbO_3$, to resistance against photorefractive damage[27] when a 50% domain duty cycle is employed. RMS duty cycle errors must be maintained below 37.5% to achieve at least 50% of ideal conversion efficiency. To achieve resistance to photorefractive damage comparable to $MgO:LiNbO_3$, we estimate that RMS duty cycle errors need to be kept below 1%.

To maximize duty cycle uniformity and obtain the required mean duty cycle, two strategies are employed. This section presents one of these strategies, which is to design an electrode and insulator geometry and poling waveform that minimizes the influence of defects. The other strategy is to eliminate defects through advancements in fabrication technology, and is presented in Section 2.3.

An important tool for generating designs that minimize the influence of defects is a computational model that permits simulation of the poling process. Through simulation, design parameters can be iterated until a design is obtained that achieves the desired domain duty cycle and has a low sensitivity to defects.

The kernel of the computational model is an equation yielding domain wall duty cycle as a function of time, referred to as the equation of domain wall motion,

$$DC_d(t) = \frac{2}{\Lambda}\int_0^t v\left(E_0\left(DC_d(\tau);\mathbf{u}\right)\right)d\tau + DC_d(0), \tag{2.3}$$

where $DC_d(t)$ is domain duty cycle as a function of time *t*, $v(E)$ is domain wall velocity as a function of average field given in Equation (2.2), $E_0(DC_d;\mathbf{u})$ is the average field in the ferroelectric as a function of domain duty cycle obtained from Equation (A.23) in Appendix A, **u** is a vector of geometric and dielectric parameters and the poling waveform, and Λ is the domain period. The subscript "*d*" in DC_d indicates domain duty cycle, as distinguished from the subscript "*e*" in DC_e, which indicates electrode duty cycle. The kernel is used to iterate on the parameters in **u** until the desired duty cycle is least sensitive to variations in both **u** and the poling pulse duration.

The design process is essentially a numerical optimization procedure. It begins with a guess for **u** and $DC_d(0) = DC_e$. Next compute the average substrate field using Equation (A.23) and then the domain wall velocity using Equation (2.2). Using an appropriate choice of time step, compute the new domain duty cycle. If **u** is time-dependent, update its values. Repeat the procedure until the desired duty cycle is obtained. The time at which the desired duty cycle is obtained is the nominal poling time associated with **u**, t_{pole}. Compute the sensitivity *S* of domain duty cycle to variations in **u** and t_{pole}, using for example

$$S\left(\mathbf{u};t_{pole}\right) = \sqrt{\left[\frac{\partial}{\partial t}\ln\left(DC_d(\mathbf{u};t)\right)\Big|_{t=t_{pole}}\right]^2 + \sum_{i=1}^{n}\left[\frac{\partial}{\partial \mathbf{u_i}}\ln\left(DC_d(\mathbf{u};t)\right)\Big|_{\mathbf{u}}\right]^2}. \tag{2.4}$$

Iterate on the parameters in **u** to minimize *S*. These parameters will result in a minimum-sensitivity design for the desired domain duty cycle.

In the case where **u** is time invariant (e.g. a constant poling voltage is used), the optimization procedure can be made faster because the computation of domain duty cycle as a function of time can be performed in a straightforward manner. The procedure is as follows: First, generate a vector of domain duty cycles with values between DC_e and 50%. Second, generate a vector of domain wall velocities for each of the domain duty cycles using Equations (A.23) and (2.2). Third, generate a vector of time values using

$$t_0 = 0;$$

$$t_i = t_{i-1} + \Lambda \frac{DC_{d_i} - DC_{d_{i-1}}}{v_i + v_{i-1}}, \tag{2.5}$$

where $i = 1 \ldots \text{rows}(DC_d) - 1$. Calculate the sensitivity at the final time step and adjust **u** as in the more general case.

Given **u**, domain wall velocity and domain duty cycle can be plotted and compared against experimental data. Note that domain wall velocity is proportional to poling current, and domain duty cycle is proportional to the charge delivered. Figure 2.13 below shows good qualitative agreement between the model's predictions and experimental data. The voltage, current, and charge waveforms were obtained for a 500-µm-thick

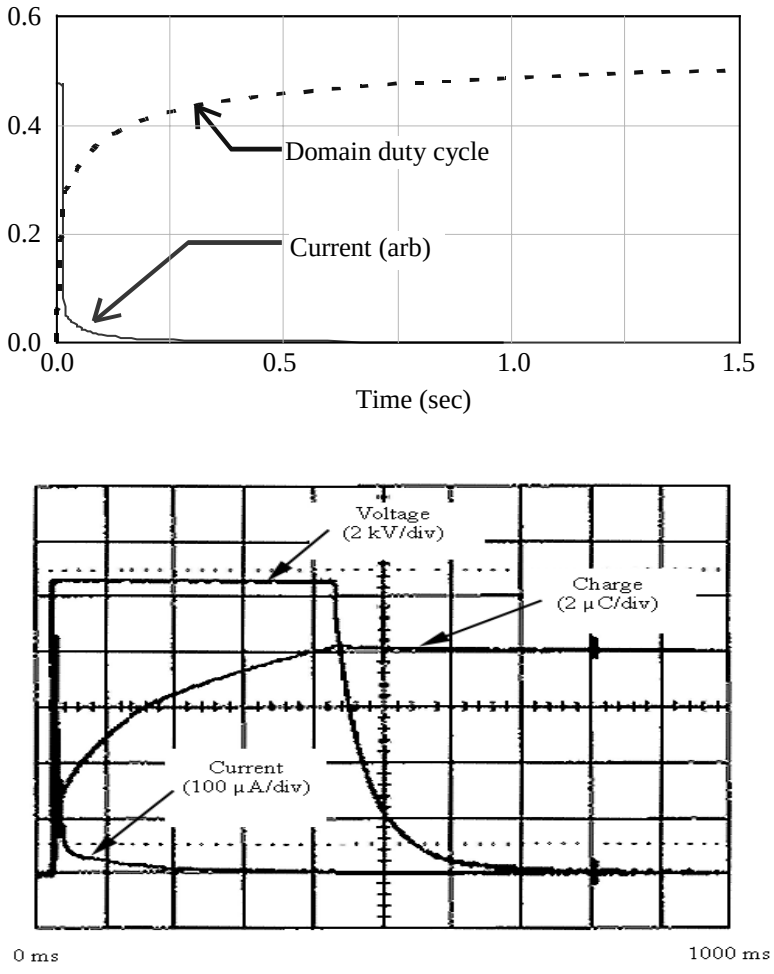

Figure 2.13. (top) Calculated poling current and domain duty cycle versus time. (bottom) Measured poling current and charge versus time. (Charge is proportional to domain duty cycle.) The model predicts self-terminating behavior seen experimentally as well as details of poling current.

sample with a 0.5-µm-thick spin-on-glass insulator and 2.7-µm-wide electrodes with a 6.5-µm period. The remarkable similarity in the current-versus-time profile indicates the predictive capabilities of the model. Figure 2.13 also shows that the domain patterning process is self-terminating both in theory and in practice when the proper poling field is chosen.

To identify the optimum poling voltage, the fractional change in domain wall velocity from the beginning of poling to the desired domain duty cycle should be used. An example of the effect of poling voltage on the fractional change in domain wall velocity can be seen in Figure 2.14. In this example, the sample is 500-µm thick, has a 6.5-µm period with 1-µm-wide electrodes, and is covered with a 0.5-µm-thick spin-on-glass insulator. With an applied voltage of 10.0 kV, domain-wall velocity decreases by a factor of 11 as the domain duty cycle increases from 15% to 30%. With an applied voltage of 11.0 kV, domain-wall velocity decreases by a factor of 110. The optimum poling voltage, 10.7 kV results in a 3000-fold reduction in domain wall velocity. At 10.7 kV, the internal field is initially 21.4 kV/mm and decreases to 20.6 kV/mm as the domain grows. The large change in domain wall velocity is due to the high velocity-field contrast at 20.75 kV/mm. When using the optimum poling voltage, domain motion slows dramatically as it approaches the design-target duty cycle, providing a wide tolerance on the duration of the poling pulse.

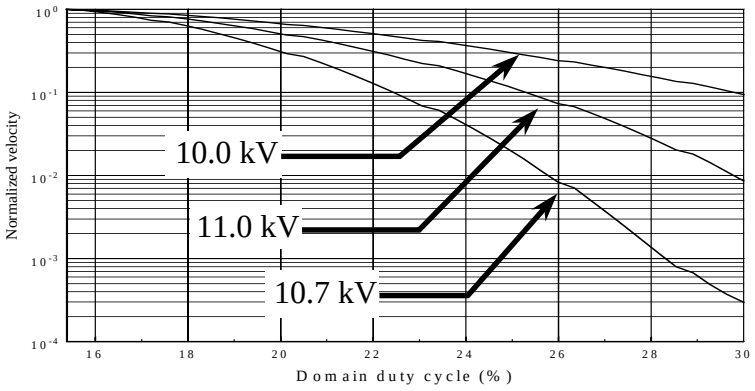

Figure 2.14. Normalized domain wall velocity versus time for three different choices of electrode voltage. An electrode voltage of 10.7 kV/mm results in a 3000-fold reduction in domain wall velocity as the domain duty cycle increases from 15% to 30%.

The predictive power of the model facilitates the design of electrode and insulator configurations. An important parameter is the electrode width needed to create a 50% domain duty cycle. The computational part of the model provides a means for simultaneously optimizing both the initial poling voltage and the electrode width in order to achieve a specified domain duty cycle. Figure 2.15 shows the results of such a calculation, where a 0.5-µm-thick spin-on-glass insulator covers the periodic electrodes and sample surface.

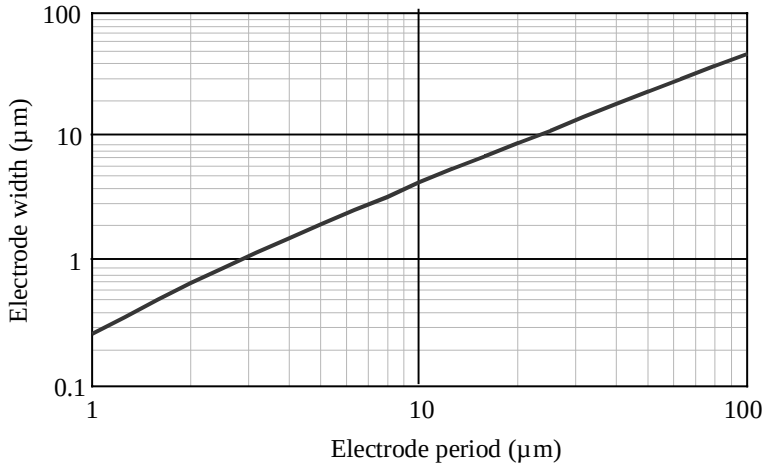

Figure 2.15. Electrode width versus electrode period to achieve 50% domain duty cycle for 500-µm-thick substrates with 0.5-µm-thick spin-on-glass insulator poled at 20.75 kV/mm.

2.3. Fabrication of electric field periodically-poled lithium niobate

This section presents the processing steps used to obtain 6.5-µm-period PPLN over an entire 0.5-mm-thick 75-mm-diameter wafer. Previously, excessive domain merging limited the maximum length of PPLN devices with this period to 6 mm.[28] PPLN fabrication with uniform domain pattern quality over an entire wafer permits fabrication of devices over 50 mm in length. This period quasi-phase-matches 1064 nm Nd:YAG second harmonic generation at ~200°C, a temperature which was expected to be high enough to suppress photorefractive damage.

This section first describes wafer preparation, emphasizing the motivation for some of the steps taken. The poling procedure is discussed next, including details on poling waveform design. Finally, the resulting material is described.

The +*z* face of an optical grade *z*-cut lithium niobate wafer was lithographically patterned with a periodic array of sputtered nichrome stripes with the grating **k** vector parallel to the crystallographic *x* axis. The wafers, made by Crystal Technology, Inc., had a 500-µm nominal thickness and a 76.2-mm diameter. The nichrome composition was 80% Ni, 20% Cr. Nichrome was chosen because it provided the greatest nucleation site density (NSD) of any of the electrode materials tested. The +*z* face was chosen because nichrome exhibited higher NSD on the +*z* face than the –*z* face. Nichrome's NSD was approximately one nucleus per period-squared for the 6.5-µm period used here. Below this value, the model suggests that domain pattern quality will suffer greatly.

The nichrome stripes were 50 nm thick, 1 µm wide, 60 mm long, and had a period of 6.5 µm. With 1-µm-wide stripes, the electric-field poling model predicts a domain duty cycle of 35%. Although a 50% domain duty cycle is preferable, the lower duty cycle was chosen to reduce the coalescence of domains between the electrodes.

The metallized +*z* face was overcoated with a 0.5-µm-thick spin-on-glass (Allied Signal) insulator cured at 350°C in air for 8 h. Spin-on-glass was chosen after finding that photoresist lacked either adequate resistivity when baked in the usual manner, or adequate dielectric strength when super-baked (180°C). An annular electrolyte-contact window, 55 mm in diameter and 2-mm wide, was opened in the insulator with hydrofluoric acid and a photoresist mask. Two additional contact windows were added to compensate for discontinuous metal stripes caused by defects in lithography.

Next, the thickness of the wafer was measured to determine the voltage required for the desired poling field. The wafer was then loaded into an electrolyte-contacting fixture of a type previously reported[11]. The electrolyte used was a saturated solution of lithium chloride in water. The electrolyte uniformly contacted the –*z* face. On the +*z* face, the electrolyte uniformly contacted the insulator and the metal stripes were contacted via the electrolyte contact windows.

The assembled fixture was connected to a Trek Model 20/20 high voltage amplifier driven by a SRS DS345 arbitrary waveform generator. The Trek is a voltage-regulated high-voltage amplifier with a nominal current limit of 20 mA. The voltage across the contact fixture was recorded using the Trek's voltage monitor output and a LeCroy 9304M oscilloscope. The current through the wafer was monitored using a 1-kΩ series

resistor to ground. The SRS was programmed to apply 21.5 kV/mm to the wafer to maximize domain NSD[5]. When the poling current rose to the Trek's current limit, the applied field fell to 20.9 kV/mm. The pulse was delivered for 140 ms to pole the material and then stepped to 19.5 kV/mm for 10 ms, and then ramped to 0 kV/mm over 60 ms to prevent backswitching.

The wafer was removed from the fixture, the insulator and metal were etched away, and the wafer was etched in hydrofluoric acid to reveal the overall uniformity of the domain pattern. This procedure was repeated for a second wafer. Both wafers showed good domain pattern uniformity. The *y* face of a sample taken from one of these wafers was polished and etched in hydrofluoric acid to reveal the domain quality through the volume of the material. Figure 2.16 shows the etched *y* face through the 0.5-mm-thick sample. Close visual inspection shows good domain uniformity with a duty cycle close to the 35% predicted by the model. Approximately 5% of the domains merged at depths of 100 to 150 µm.

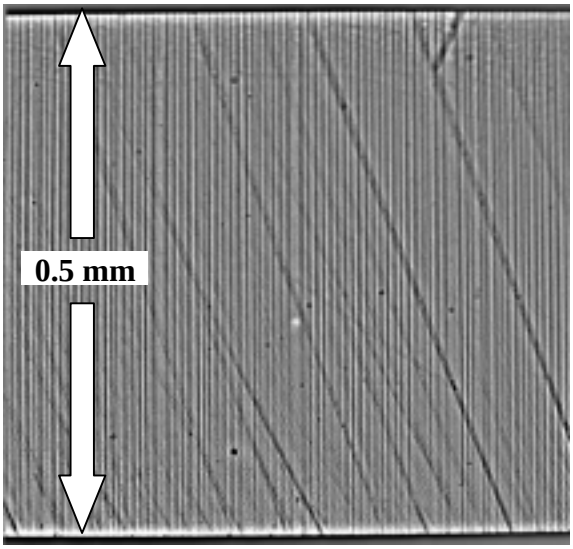

Figure 2.16. Etched *y*-face of 0.5 mm thick periodically poled $LiNbO_3$ showing 6.5 µm period domains. The domain duty cycle is approximately 35%. (Diagonal features are polishing scratches).

2.4. Summary

This chapter presented a model of domain kinetics during electric field periodic poling in $LiNbO_3$. The model consists of a descriptive part and a computational part. The

descriptive part of the model provides a set of simplifying assumptions about periodic poling, based on observations taken from the literature and our own experiments. The descriptive part of the model also provides an idealized picture of the stages of domain kinetics. Each of these stages was discussed relative to actual experimental observations.

The computational part of the model provides an equation of domain wall motion that is used to optimize fabrication and process parameters, not only to attain a specified domain duty cycle, but to also reduce susceptibility to defects. The computational part combines the electrostatics of periodic poling, discussed in Appendix A, with the velocity-field function of $LiNbO_3$. We showed that the model has the ability to predict experimental outcomes, including poling current and domain duty cycle, and that the model can be used as a design and simulation tool.

Finally, this chapter presents a recipe for fabricating 0.5-mm-thick 75-mm-diameter PPLN with a 6.5-μm-domain period, using the model to aid in the selection of materials, in specifying the electrode width, and in designing the poling waveform. The next chapter presents the nonlinear-optical performance of 53-mm-long samples obtained from these two wafers.

References for Chapter 2

1 M. Yamada, N. Nada, M. Saitoh *et al*., "First-order quasi-phased matched $LiNbO_3$ waveguide periodically poled by applying an external field for efficient blue second-harmonic generation," Applied Physics Letters **62** (5), 435-6 (1993).

2 L. E. Myers, R. C. Eckardt, M. M. Fejer *et al*., "Quasi-phase-matched optical parametric oscillators in bulk periodically poled $LiNbO_3$," Journal of the Optical Society of America B (Optical Physics) **12** (11), 2102-16 (1995).

3 A. Harada and Y. Nihei, "Bulk periodically poled MgO-$LiNbO_3$ by corona discharge method," Applied Physics Letters **69** (18), 2629-31 (1996).

4 L. Goldberg, W. K. Burns, and R. W. McElhanon, "Difference-frequency generation of tunable mid-infrared radiation in bulk periodically poled $LiNbO_3$," Optics Letters **20** (11), 1280-2 (1995).

5 G. D. Miller, R. G. Batchko, M. M. Fejer *et al*., "Visible quasi-phase-matched harmonic generation by electric-field-poled lithium niobate," Proceedings of the SPIE - The International Society for Optical Engineering **2700**, 34-45 (1996).

6 G. D. Miller, R. G. Batchko, W. M. Tulloch *et al*., "42%-efficient single-pass CW second-harmonic generation in periodically poled lithium niobate," Optics Letters **22** (24), 1834-6 (1997).

7 K. Mizuuchi and K. Yamamoto, "Harmonic blue light generation in bulk periodically poled $LiTaO_3$," Applied Physics Letters **66** (22), 2943-5 (1995).

8 K. Mizuuchi, K. Yamamoto, and M. Kato, "Generation of ultraviolet light by frequency doubling of a red laser diode in a first-order periodically poled bulk $LiTaO_3$," Applied Physics Letters **70** (10), 1201-3 (1997).

9 Zhu Shi-ning, Zhu Yong-yuan, Yang Zhen-ju *et al*., "Second-harmonic generation of blue light in bulk periodically poled $LiTaO_3$," Applied Physics Letters **67** (3), 320-2 (1995).

10 C. Baron, H. Cheng, and M. C. Gupta, "Domain inversion in $LiTaO_3$ and $LiNbO_3$ by electric field application on chemically patterned crystals," Applied Physics Letters **68** (4), 481-3 (1996).

11 L. E. Myers, R. C. Eckardt, M. M. Fejer *et al*., "Quasi-phase-matched optical parametric oscillators in bulk periodically poled $LiNbO_3$," Journal of the Optical Society of America B (Optical Physics) **12** (11), 2102-16 (1995).

12 L. E. Myers, in *Quasi-phasematched Optical Parametric Oscillators in Bulk Periodically Poled Lithium Niobate* (Stanford University Doctoral Dissertation, 1995), pp. 43-44.

13 A.L.Alexandrovski and V.V.Volkov, "Formation of domains in lithium niobate in temperature range of 20-200C", Moscow State University, Department of Physics, Preprint No 8, 1997.

14 V. Ya. Shur in *Ferroelectric thin films: synthesis and basic properties*, edited by Carlos Paz de Araujo, James F. Scott and George W. Taylor (Gordon and Breach Publishers, Amsterdam, 1996), p. 153 ff.

15 A. L. Aleksandrovski, private communication, 1997.

16 R. C.Miller and A. Savage, Phys. Rev. **115**, 1176 (1959).

17 M. Hayashi, "Kinetics of domain wall motion in ferroelectric switching. I. General formulation," Journal of the Physical Society of Japan **33** (3), 616-28 (1972).

18 E. Fatuzzo and W. J. Merz, in *Ferroelectricity* (North-Holland Publishing Company, Amsterdam, 1967), p. 193.

19 L. E. Myers, in *Quasi-phasematched Optical Parametric Oscillators in Bulk Periodically Poled Lithium Niobate* (Stanford University Doctoral Dissertation, 1995), p. 59.

20 Chao Shiuh, W. Davis, D. D. Tuschel *et al*., "Time dependence of ferroelectric coercive field after domain inversion for lithium-tantalate crystal," Applied Physics Letters **67** (8), 1066-8 (1995).

21 V. Gopalan and M. C. Gupta, "Origin of internal field and visualization of 180 degrees domains in congruent $LiTaO_3$ crystals," Journal of Applied Physics **80** (11), 6099-106 (1996).

22 V. Gopalan and M. C. Gupta, "Internal fields in lithium tantalate single crystals," Proceedings of the SPIE - The International Society for Optical Engineering **2700**, 28-33 (1996).

23 V. Gopalan and M. C. Gupta, "Observation of internal field in $LiTaO_3$ single crystals: its origin and time-temperature dependence," Applied Physics Letters **68** (7), 888-90 (1996).

24 V. Gopalan and M. C. Gupta, "Origin and characteristics of internal fields in $LiNbO_3$ crystals," Ferroelectrics **198**, 49-59 (1997).

25 G. D. Miller, Poster presentation at the Center for Nonlinear Optical Materials Annual Review, August, 1994.

26 M. M. Fejer, G. A. Magel, D. H. Jundt *et al*., "Quasi-phase-matched second harmonic generation: tuning and tolerances," IEEE Journal of Quantum Electronics **28** (11), 2631-2654 (1992).

27 M. Taya, M. C. Bashaw, and M. M. Fejer, "Photorefractive effects in periodically poled ferroelectrics," Optics Letters **21** (12), 857-9 (1996).

28 V. Pruneri, R. Koch, P. G. Kazansky *et al*., "49 mW of CW blue light generated by first-order quasi-phase-matched frequency doubling of a diode-pumped 946-nm Nd:YAG laser," Optics Letters **20** (23), 2375-7 (1995).

CHAPTER 3. NONLINEAR-OPTICAL PERFORMANCE

Chapter 2 presented a method for fabricating 53-mm-long 0.5-mm-thick PPLN samples with a 6.5-μm-domain period using electric field periodic poling. This period is suitable for quasi-phase-matched SHG of 532-nm radiation at a calculated phase-matching temperature of 195.6°C, computed using the Sellmeier equation presented in Reference 1. This period is also suitable for use in an optical parametric oscillator (OPO) pumped at 532 nm. The length of these samples provides the conversion efficiency needed for the development of simple coherent sources of visible light and the gain needed for low-threshold OPO's. By measuring the nonlinear-optical performance of these samples, we verified that electric field periodic poling retains the intrinsic properties of $LiNbO_3$ and produces a material suitable for use in visible light applications.

This Chapter first presents the results of cw single-pass SHG experiments that produced 2.7 watts of 532 nm radiation at 42% efficiency, the highest cw power and efficiency reported to date.[2] The second section of this Chapter presents the results of singly-resonant OPO (SRO) experiments where a record low threshold of 930 mW was achieved and temperature tuning from 917 nm to 1266 nm was demonstrated.[3,4] The final section of this Chapter presents findings regarding green-induced infrared absorption.[5]

3.1. Single-pass cw SHG

Single-pass cw SHG performance was measured both in the low-conversion limit and in the presence of pump depletion using 1064 nm Nd:YAG input radiation. In the low-conversion limit, the temperature tuning characteristics demonstrated that domain pattern quality, material dispersion, and temperature were uniform over the length of the sample. Measurements of harmonic output power versus fundamental input power demonstrated that the effective nonlinearity was consistent with visual characterization of the domain duty cycle. Increases in fundamental input power resulted in pump depletion and revealed new behaviors at harmonic power levels exceeding 1 watt.

3.1.1. Low conversion limit performance

Seven 53-mm-long, 3-mm-wide samples were cut from the two wafers discussed in Chapter 2. An image of two of these samples is shown in Figure 3.1. The sample endfaces were polished but left uncoated for characterization by SHG. The TEM_{00} output of a Lightwave Series 122 single frequency Nd:YAG laser was loosely focused through several of the samples to determine their phase-matching characteristics and effective nonlinear coefficients. Figure 3.2 shows a SHG temperature-tuning curve for one of these samples. The observed phase-matching temperature was 199.5°C, which compares favorably with a predicted phase-matching temperature of 195.6°C that was determined with a recently published temperature-dependent Sellmeier equation for $LiNbO_3$ and with thermal expansion taken into account[1]. The theoretical phase-matching curve for a 53-mm-long sample was shifted in temperature in Figure 3.2 for comparison with the 199.5°C experimental phase-matching data. The excellent agreement indicates that domain periodicity, material dispersion, and the oven temperature profile were uniform over the entire 53-mm-sample length.

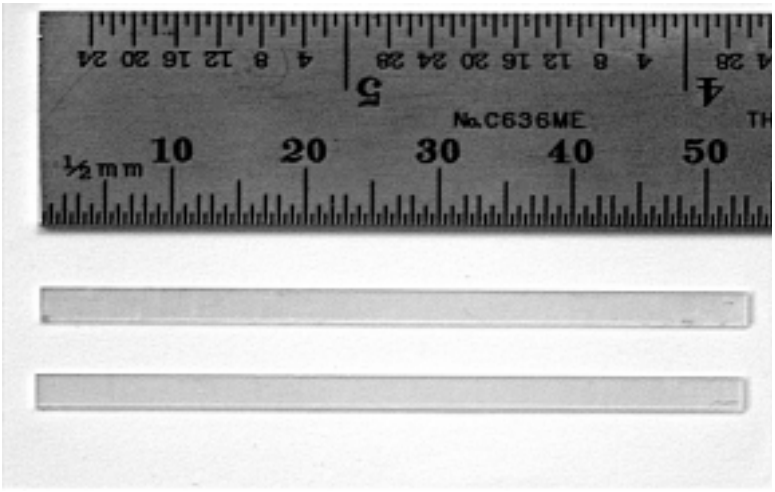

Figure 3.1. Two 0.5-mm-thick PPLN samples 53-mm long and 3-mm wide with a domain period of 6.5 µm.

Using measurements of conversion efficiency in the loose-focus low-power limit, beam dimensions, and crystal length, the effective nonlinear coefficient was calculated to be 14 pm/V, 78% of the value for an ideal first-order QPM grating and 88% of the 16 pm/V expected for a uniform 35% duty cycle. Both the predicted and the measured

single-pass conversion efficiencies for confocally focused interactions were 8.5%/watt, versus 14%/watt predicted for perfect first order QPM.

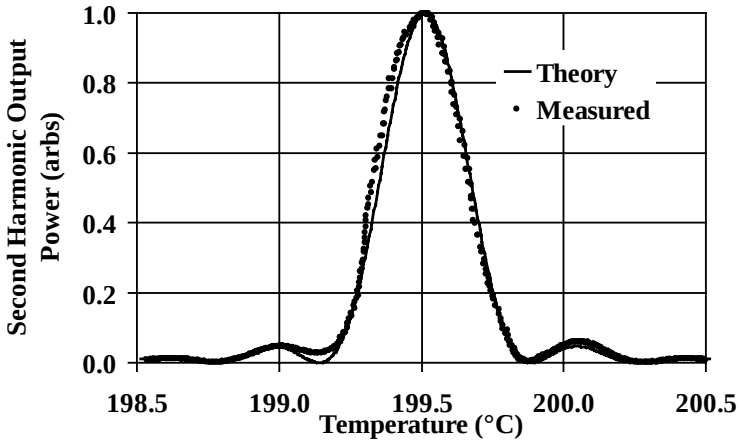

Figure 3.2. 532-nm output power [in arbitrary units (arbs)] versus temperature for Nd:YAG SHG. The dots are experimental data and the solid curve is the theoretical plane-wave curve for a 53-mm sample, shifted to the same peak phase-matching temperature. The good agreement between data and theory indicates that the sample phase matches over the full 53-mm length.

3.1.2. High power performance

We next tested these samples at higher power levels by single-pass cw SHG using an 8-watt cw Lightwave Series 220 Nd:YAG laser ($M^2 \approx 1.3$). During these measurements, absorption by the fundamental and harmonic beams gave rise to thermal lensing and apparent shifts in the phase-matching temperature. To compensate for these effects, harmonic output power was maximized for each value of input fundamental power by adjusting the input beam waist size and location and the oven temperature. Figure 3.3 shows the generated 532-nm output power versus 1064-nm input power for one sample in which second-harmonic output power was maximized for each value of fundamental input power. All powers are internal to the sample and corrected for Fresnel reflection at the endfaces. Second harmonic power of 2.7 watts was generated for 6.5 watts of input; the internal conversion efficiency was 42%. This conversion efficiency is more than an order of magnitude above that previously obtained for cw single-pass SHG in a bulk material[6].

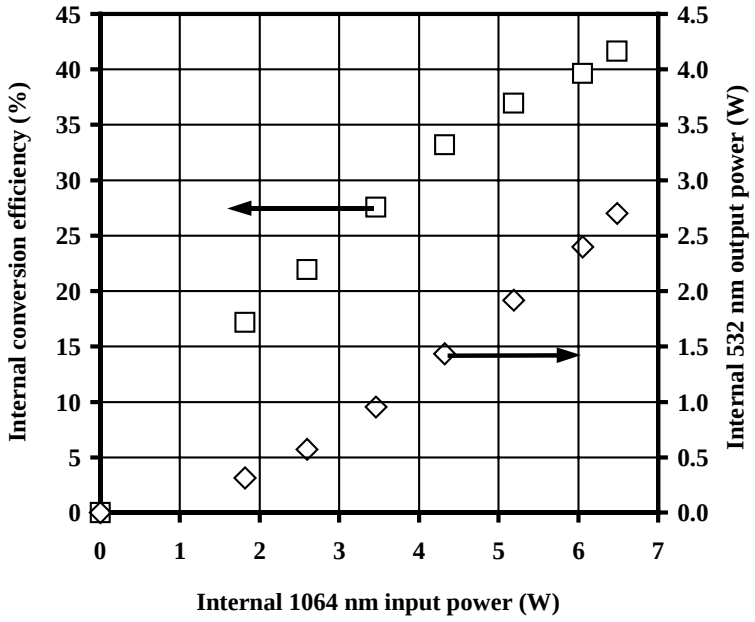

Figure 3.3. Measured cw 532-nm output power internal to exit face of sample versus 1064-nm input power internal to the input face of the sample. The conversion efficiency for cw single-pass Nd:YAG SHG was 42% at 6.5 watts of input power yielding 2.7 watts of 532-nm output power.

For 1064-nm input powers exceeding ~3 watts, both the 532-nm and 1064-nm output beams exhibited pointing instability when the temperature was tuned to phase-matching. The instability was transient, decaying away in less than 1 h. The pointing instability was anisotropic, and the beam deviated parallel to the crystalline *z* axis. The anisotropic nature of this instability is suggestive of photorefractive damage.

For 1064-nm input powers exceeding ~5.5 watts, both the 532-nm and 1064-nm output beams exhibited spot size instability when the temperature was tuned to phase matching. The fundamental output beam did not exhibit this instability when the temperature was tuned away from phase matching. The presence of a significant amount of second-harmonic, with its higher absorption coefficient, can be expected to give rise to increased thermal self-focusing, which can in turn cause spot-size instabilities and eventually filament formation. With a fundamental input power of 6.5 watts, the sample whose data is shown in Figure 3.3 operated for approximately 1 h before damage occurred due to the formation of a beam filament after a mechanical shock to the optical table.

Summarizing, 53-mm-long electric field periodically poled $LiNbO_3$ with a 6.5-µm-domain period was shown to quasi-phase-match over its entire length, had 8.5%/watt single-pass conversion efficiency in the low-power limit, and produced 2.7 watts of cw 532 nm output with 42% single-pass efficiency.

3.2. Singly-resonant OPO

The broad tunability of PPLN OPO's makes them attractive for spectroscopy, remote sensing, and other applications.[7,8] By selecting the correct combination of QPM grating period and phase-matching temperature, 532-nm-pumped PPLN OPO's offer the opportunity of producing visible wavelengths while still providing access to idler wavelengths out to 5 µm. The OPO presented here utilized the 6.5-µm-domain period PPLN used for the SHG experiments described in the previous section and was tunable from 917 nm to 1266 nm. The high nonlinearity afforded by the 53-mm-long PPLN samples and the quality of their domain structure permitted cw singly resonant operation with a 930 mW internal threshold. Previous reports of 532-nm-pumped QPM SRO's relied on shorter crystals and required use of a Q-switched pump.[9]

The first cw SRO was introduced by Yang *et al.* in 1992 and utilized KTP as the nonlinear medium.[10,11] At the time, KTP offered the best available combination of material properties such as high gain, low absorption loss, suitable temperature-acceptance bandwidth and high damage threshold. By pumping at 532 nm with a resonantly-doubled, single-frequency cw lamp-pumped Nd:YAG laser, an oscillation threshold of 4.3 watts was achieved. This work demonstrated the high spectral purity, narrow linewidth and high efficiency of cw SRO's, as well as their greater stability compared to doubly resonant OPO's with respect to pump-frequency and cavity-length fluctuations. However, due to the limitations of Type-II non-critical phase matching, the KTP SRO could not be significantly tuned.

In 1996 Bosenberg *et al.* demonstrated the first cw quasi-phase-matched SRO.[12,13] The pump source for this device was a 1064 nm Nd:YAG laser, and the nonlinear crystal was PPLN with a 29.75 µm domain period. With a QPM nonlinear coefficient of $d_Q \approx 14.4$ pm/V, substantially larger than Type-II noncritically-phase-matched KTP [$d_{32} = 3.6$ pm/V],[7] the PPLN SRO reached an oscillation threshold of 3.6 watts. In comparing

this threshold to that of the 532-nm-pumped device, it should be noted that the gain of an OPO with confocal focusing goes as λ_{pump}^{-3}. With this period PPLN, the idler tuned from 3-4 µm, a significant improvement over that of the KTP SRO. The milestones of their work were 80% conversion efficiency, 96% pump depletion, and the maintenance of single-longitudinal-mode oscillation in a ring SRO when pumped with a multi-longitudinal-mode laser. At that time, fabrication of long samples of PPLN was not practical for domain periods shorter than ~20 µm, so that efficient cw QPM was therefore limited to the mid-infrared spectrum.

The experimental set-up is shown in Figure 3.4. The pump laser was a Spectra Physics *Millennia*, a 5-watt cw 532-nm single-transverse-mode multi-longitudinal-mode intracavity-doubled diode-pumped Nd:YVO_4 laser. The pump beam was mode-matched into a four-mirror 'bow-tie' ring cavity which formed the SRO resonator. The cavity was comprised of two 20-cm radius-of-curvature mirrors and two flat mirrors. The total empty-cavity optical path length was 116.6 cm. All four mirrors were highly reflecting from 900-1000 nm, and the combined mirror transmission at 1100-1200 nm was approximately 90%, thus making the cavity resonant only at the signal wavelengths. Both end faces of the PPLN crystal were antireflection (AR) coated for the wavelengths from 800 nm to 1100 nm. The coatings were evaporation deposited at a substrate temperature of 100°C to ensure good adhesion when heating the crystal during operation. The PPLN crystal was mounted in an oven located at the waist of the SRO cavity. The SRO cavity mode had a 64-µm waist and was thus confocally focused in the PPLN crystal. The SRO optics were not optimized for transmission at 532 nm, with each mirror and AR-coated crystal surface having a pump transmission of ~88%. The combined pump power loss from the SRO input mirror and the AR-coated PPLN input face was 22.6%.

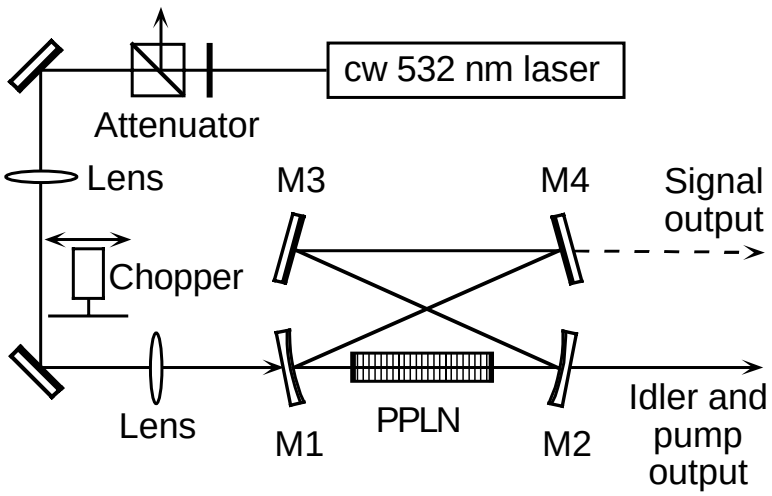

Figure 3.4. Schematic diagram of the four-mirror 'bow-tie' ring SRO. The pump was a cw 532-nm 5-watt frequency-doubled Nd:YVO_4 laser. The cavity utilized two 20-cm radius-of-curvature mirrors (M1, M2) and two planar mirrors (M3, M4). All mirrors M1-M4 were HR at 900-1000 nm. The PPLN crystal was 53 mm long, 0.5 mm thick and had a grating period of 6.5 μm for first order QPM of the 532 nm pump at temperatures above 198 °C.

Absorption of 532 nm pump radiation in the PPLN crystal caused thermal lensing and beam pointing instability of the transmitted pump and the idler beams. With increasing 532 nm power, these effects intensified and oscillation became unstable. We reduced these losses by modulating the pump with a 50%-duty-cycle mechanical chopper at 2 kHz. With lower average 532-nm power in the PPLN, lower threshold, stable oscillation and fixed spot sizes of the transmitted pump and idler were observed. Figure 3.5 is a plot showing 1192 nm internal idler power (squares) and pump depletion (circles) versus internal pump power. Since the SRO mirrors and PPLN AR coatings were not optimized for transmission at 532 nm, the pump power levels are presented in terms of power internal to the PPLN crystal. Internal idler power is determined as the idler power measured at the output of mirror M2 (see Figure 3.4) adjusted by a factor of 4.3 to account for Fresnel and mirror losses. The data in Figure 3.5 was taken with the pump modulated as described above. Both pump and idler power levels represent peak power during the approximately square-wave chopper cycle. The oscillation threshold was 930 mW internal to the PPLN crystal, 1.06 watts at the input face of the PPLN crystal, and 1.2 watts at the SRO input mirror. With 3.3 watts of internal pump power, the internal idler power was 820 mW, giving 78% idler quantum slope efficiency internal to the PPLN crystal. Residual loss limited pump depletion to 60% and internal quantum

efficiency to 56% for 3.3 watts of internal pump power. The PPLN crystal's large parametric gain of ~8.5%/watt[14] allowed us to achieve cw SRO operation with two other cw 532 nm pump lasers: a 2-watt Spectra Physics *Millennia II*, and a 9-watt Nd:YAG Lightwave *Series 220* laser that was single-pass frequency-doubled using one of the other 6.5-µm-period 53-mm-long PPLN samples we fabricated.

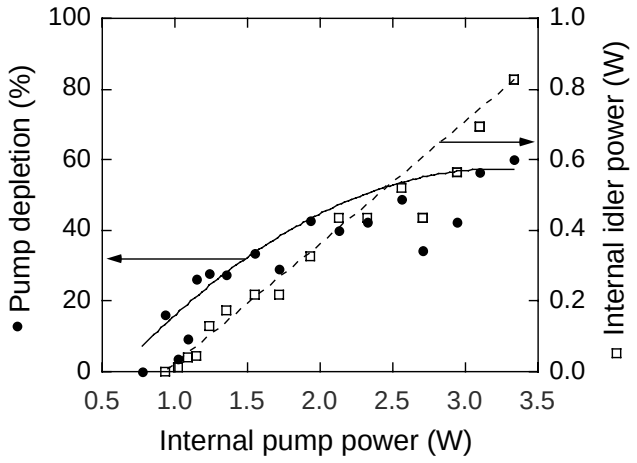

Figure 3.5. Pump depletion (circles) and idler power internal to the PPLN crystal (squares) versus pump power internal to the PPLN crystal. In order to reduce thermal loading of the PPLN at 532 nm, a 50%-duty-cycle mechanical chopper was used to modulate the pump. Pump and idler power levels represent peak power during the chopper cycle. The oscillation threshold was 930 mW. The maximum idler power was 820 mW at 1192 nm with 3.3 watts of pump.

We extracted signal power from the SRO by replacing mirror M4 (see Figure 3.4) with a planar 96% reflector at the 961 nm signal wavelength. Figure 3.6 shows plots of output power for both the 961-nm signal and 1192-nm idler versus pump power internal to the PPLN for this output-coupled cavity. Both the signal and idler power were measured at the outputs of mirrors M4 and M2, respectively. The pump was again modulated at 2 kHz with a 50% duty cycle, and pump, signal, and idler power levels represent peak power during the chopper cycle. With the added mirror loss the oscillation threshold increased to ~1.8 watts internal to the PPLN. No significant beam-steering or thermal lensing effects were observed in the output beams for internal peak pump powers up to the available 3 watts.

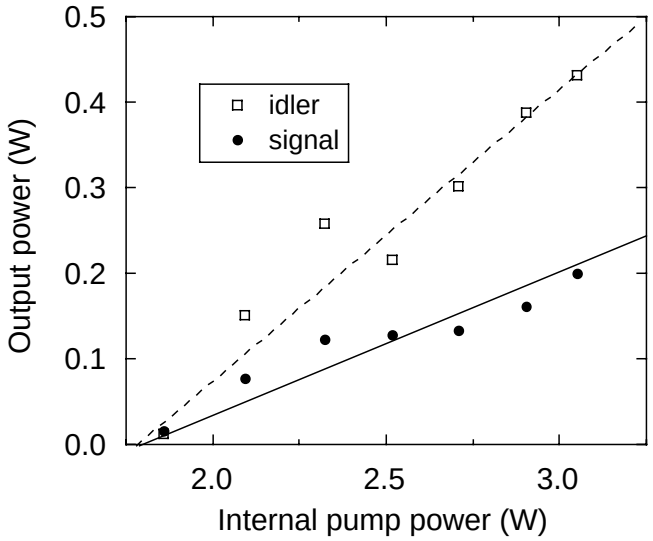

Figure 3.6. Output power of the 961 nm signal (circles) and 1192 nm idler (squares) versus pump power internal to the PPLN crystal for the output-coupled cavity. A planar reflector (R=96% at 961 nm) was used as an output coupler for the resonated signal. Here, as in Figure 3.5, the pump was modulated with a 50%-duty-cycle chopper and power levels represent peak power during the chopper cycle. With the additional mirror transmission, the oscillation threshold increased to 1.8 watts.

Figure 3.7 shows the SRO output wavelengths as a function of the temperature of the PPLN crystal. Using the mirror set described in Figure 3.4, the crystal was heated from 212°C to 260°C, achieving signal tuning from 988 nm to 917 nm, and idler tuning from 1151 nm to 1267 nm (dots). Near-degenerate oscillation, with signal tuning from 1059 nm to 992 nm, and idler tuning from 1065 nm to 1147 nm, was achieved by replacing both flat cavity mirrors with flat 1064 nm high-reflector mirrors and heating the crystal from 200°C to 213°C (crosses). We noted the initiation of double resonance for operation very near degeneracy, with signal and idler mode hopping. Two theoretical tuning curves are also shown in Figure 3.7. These curves are calculated from the temperature-dependent Sellmeier equations for the index n_e in congruent $LiNbO_3$ as published by Edwards *et al.*[15] (dashed curve) and recently by Jundt[1] (solid curve). Good agreement is observed with the Sellmeier equation of Jundt while, as has been reported elsewhere, the actual phase-matching temperature for SRO degeneracy is approximately 15°C higher than that calculated by Edwards *et al.*[7,8,16]

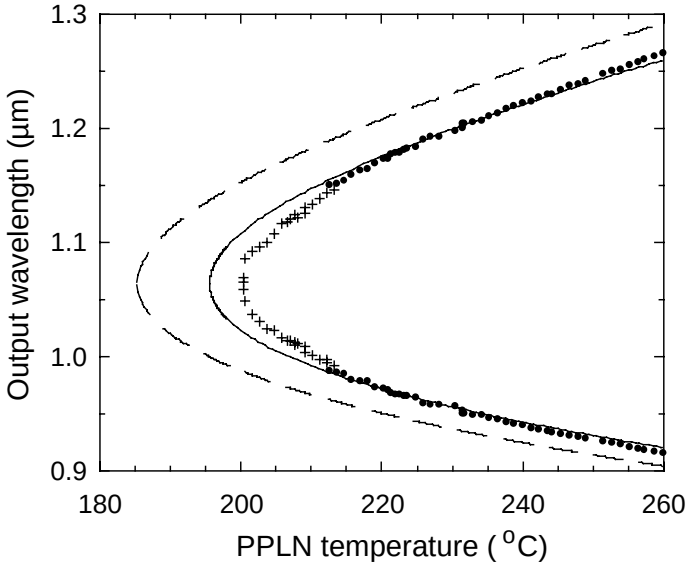

Figure 3.7. Wavelength tuning versus temperature for the SRO. The 6.5-μm-domain-period PPLN was heated from 200°C to 260 °C, tuning the output from 917-1266 nm. Two mirror sets were utilized; one set optimized for off-degenerate tuning (circles) and a second set optimized for near-degenerate tuning (crosses). Double-resonance was observed at phase matching very near degeneracy. Two theoretical tuning curves are calculated from the temperature-dependent Sellmeier equations for the index n_e in congruent $LiNbO_3$ of Edwards *et al*. (dashed curve) and Jundt (solid curve). Good agreement is found with the Sellmeier equation of Jundt.

To summarize, 53-mm-long electric field periodically poled $LiNbO_3$ with a 6.5-μm-domain period was used to construct the first reported 532-nm-pumped cw QPM SRO. The SRO operated with a multi-longitudinal-mode diode-pumped frequency-doubled Nd:YVO_4 laser. Due to the large effective nonlinear coefficient and long interaction length of the PPLN sample, the SRO had a 930 mW internal threshold, exhibited 56% conversion efficiency, and was temperature tuned from 917 nm to 1267 nm. Although 532-nm-induced IR absorption and thermal lensing limited device performance, the crystal's large parametric gain enabled simple and reliable SRO operation with a variety of commercial pump lasers.

3.3. Green-induced infrared absorption (GRIIRA)

The behavior during the SHG and SRO measurements with 532-nm powers exceeding ~1 watt was suggestive of 532-nm-induced infrared absorption in the crystal. To investigate this hypothesis, infrared loss as a function of internal green power was measured directly, and the thermal lens produced by infrared absorption was measured

with and without 532-nm radiation present. The results of these measurements are presented, followed by discussion of a method for substantially reducing GRIIRA.

The experimental set-up for measuring GRIIRA in PPLN is shown in Figure 3.8. We focused 180 mW of 1064 nm radiation from a single-frequency cw Nd:YAG laser to a 64 µm waist inside a 53-mm-long 0.5-mm-thick 6.5-µm-domain-period PPLN crystal. A 2-watt cw multi-longitudinal-mode 532 nm laser was focused to a 45 µm waist in the PPLN collinearly with the infrared beam. The crystal was heated to 216°C (non-phase-matched for SHG) and both the infrared and green beams were n_e polarized.

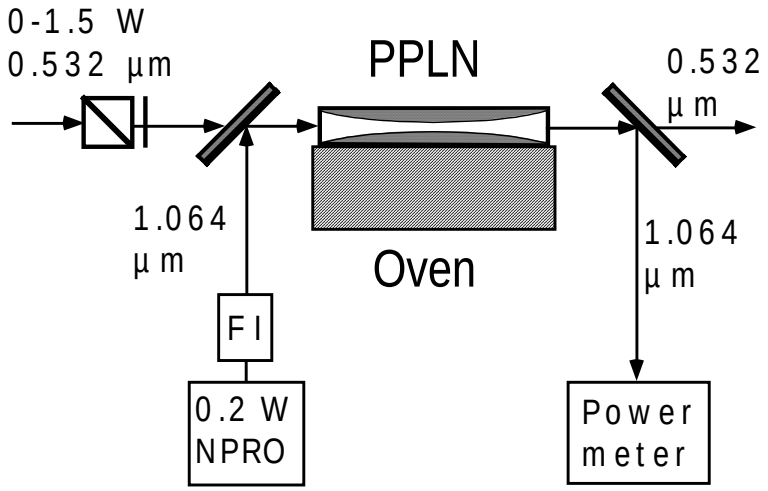

Figure 3.8. Experimental set-up for measuring GRIIRA in PPLN. A 180 mW cw 1.064 µm beam and a 2-watt 532 nm beam were collinearly focused inside a 53-mm-long PPLN crystal. The crystal temperature was 216°C, non-phase-matched for SHG. Transmitted infrared power was measured as a function of green power.

Figure 3.9 is a plot of GRIIRA versus 532-nm power internal to the PPLN. The total insertion loss of the PPLN at 1064 nm, without 532 nm light present, was ~0.5%. With green power levels of ~1 watt present internal to the PPLN, the transmitted infrared power was reduced by approximately 4%. This transmission loss scaled approximately with pump power squared for internal pump powers of 0 to 1 watt. When the 532 nm beam was blocked, the infrared transmission recovered to the original 0.5% loss with a time constant of ~20 sec. This 4% green-induced infrared loss is consistent with previously reported SRO threshold measurements using the same PPLN crystal [Ref. 4], assuming a quadratic dependence of infrared absorption on 532 nm intensity.

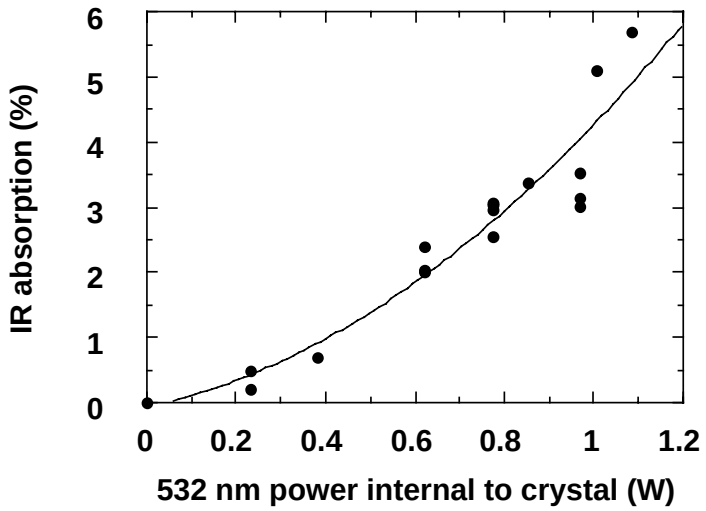

Figure 3.9. Infrared transmission loss through the PPLN crystal is plotted as a function of internal green power. For internal green power up to ~1 watt, infrared loss is seen to depend quadratically on green power.

We also examined the dependence of thermal lensing in PPLN at 1.064 µm due to the presence of infrared and green power. Light from a 9-watt cw 1.064 µm Nd:YAG laser was confocally focused to a 64 µm waist in the middle of a 53-mm-long 0.5-mm-thick 6.5-µm-domain-period PPLN crystal. The infrared power internal to the crystal was varied from 0 to 7 watts, and the crystal temperature was varied from the phase-matching temperature to 230°C. The waist size, position and far-field diffraction angle of the transmitted infrared beam were then measured. From these beam measurements an effective infrared thermal lens in the sample was determined.

As can be seen in Figure 3.10, the focal power of the infrared thermal lens, without green light present (i.e., 230°C), is linearly dependent on infrared power in the crystal (dashed curve). Next, 7 watts of infrared was focused internal to the crystal and the crystal temperature was adjusted toward the phase-matching temperature, thereby varying the amount of green light generated internal to the crystal for 0 to 1.7 watts. The infrared thermal lens focal power is seen to increase quadratically as a function of green power generated (solid curve).

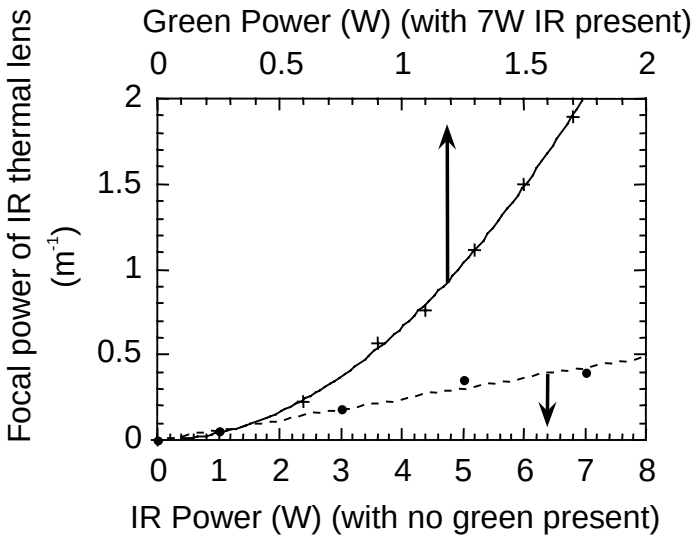

Figure 3.10. Focal power of infrared thermal lens as a function of infrared power alone (dashed curve), and as a function of internal green power with 7 watts of infrared power also present internal to the crystal (solid curve).

Recently, it was reported that GRIIRA could be nearly eliminated through photo-thermal bleaching.[17] After one hour of exposure to 1 watt of 532-nm radiation focused to a 45 µm spot in a 53-mm-long sample at 300°C, infrared absorption was reduced by a factor of two. At ~200°C (phase matching) with 5.7 watts of 1064-nm input, 532-nm harmonic power was observed to rise from 1 watt to over 1.5 watts in a stable beam over the course of several days.[18] In both cases, GRIIRA was reduced or eliminated only along the beam path. A sample annealed for two hours in the dark at 350°C experienced a four-fold reduction in green absorption and a two-fold reduction in both infrared absorption and GRIIRA. These findings suggest that annealing can be used to greatly improve the visible light power handling capability of electric field periodically poled $LiNbO_3$.

References for Chapter 3

1 D. H. Jundt, Opt. Let. **22,** 1553 (1997).

2 G. D. Miller, R. G. Batchko, W. M. Tulloch *et al*., "42%-efficient single-pass CW second-harmonic generation in periodically poled lithium niobate," Optics Letters **22** (24), 1834-6 (1997).

3 R. G. Batchko, D. R. Weise, T. Plettner *et al*., "532 nm-pumped continuous-wave singly resonant optical parametric oscillator based on periodically-poled lithium niobate," in *OSA Trends in Optics and Photonics Series. Vol.10 Advanced Solid State Lasers. From the Topical Meeting*, edited by C. R. Pollock and W. R. Bosenberg (Opt. Soc. America, Washington, DC, USA, 1997), pp. 182-4.

4 R. G. Batchko, D. R. Weise, T. Plettner *et al*., "Continuous-wave 532-nm-pumped singly resonant optical parametric oscillator based on periodically poled lithium niobate," Optics Letters **23** (3), 168-70 (1998).

5 R. G. Batchko, G. D. Miller, A. Alexandrovski *et al.*, "Limitations of high-power visible wavelength periodically poled lithium niobate devices due to green-induced infrared absorption and thermal lensing," Conf. on Lasers and Electro-Optics, Tech. Digest Series, **6**, 75-76, (Opt. Soc. Am., Washington, D.C., 1998).

6 T. Pliska, D. Fluck, and P. Guenter, "Blue-green laser by frequency doubling a master oscillator power amplifier diode laser in a $KnbO_3$ crystal," Helvetica Physica Acta **68** (5), 502-3 (1995).

7 L. E. Myers, R. C. Eckardt, M. M. Fejer *et al*., "Quasi-phase-matched optical parametric oscillators in bulk periodically poled LiNbO/sub 3," Journal of the Optical Society of America B (Optical Physics) **12** (11), 2102-16 (1995).

8 L. E. Myers, G. D. Miller, R. C. Eckardt *et al*., "Quasi-phase-matched 1.064-µm-pumped optical parametric oscillator in bulk periodically poled $LiNbO_3$," Optics Letters **20** (1), 52-4 (1995).

9 V. Pruneri, J. Webjörn, P. S. J. Russell *et al*., "532 nm pumped optical parametric oscillator in bulk periodically poled lithium niobate," Applied Physics Letters **67** (15), 2126-8 (1995).

10 S. T. Yang, R. C. Eckardt, and R. L. Byer, "Power and spectral characteristics of continuous-wave parametric oscillators: the doubly to singly resonant transition," Journal of the Optical Society of America B (Optical Physics) **10** (9), 1684-95 (1993).

11 S. T. Yang, R. C. Eckardt, and R. L. Byer, "1.9-W cw ring-cavity KTP singly resonant optical parametric oscillator," Optics Letters **19** (7), 475-7 (1994).

12 W. R. Bosenberg, A. Drobshoff, J. I. Alexander *et al*., "Continuous-wave singly resonant optical parametric oscillator based on periodically poled $LiNbO_3$," Optics Letters **21** (10), 713-15 (1996).

13 W. R. Bosenberg, A. Drobshoff, J. I. Alexander *et al*., "93% pump depletion, 3.5-W continuous-wave, singly resonant optical parametric oscillator," Optics Letters **21** (17), 1336-8 (1996).

14 In cw single-pass SHG experiments this PPLN demonstrated an effective nonlinear coefficient of 14 pm/V (78% of the ideal nonlinear coefficient), indicating an ~8.5%/watt parametric gain at degeneracy in the low-gain plane-wave limit [see Ref. 2].

15 G. J. Edwards, M. Lawrence, "A temperature-dependent dispersion equation for congruently grown lithium niobate," Opt. Quantum Electron. **16**, 373-374 (1984).

16 G. D. Miller, R. G. Batchko, W. M. Tulloch, D. R. Weise, M. Fejer, R. L. Byer, "42% efficient single-pass second harmonic generation of continuous-wave Nd:YAG laser output in 5.3 cm length periodically-poled lithium niobate," Conf. on Lasers and Electro-Opt., Tech. Digest Series, **11**, 58-59, (Opt. Soc. Am., Washington, D.C., 1997).

17 R. G. Batchko, G. D. Miller, A. Alexandrovski *et al.*, "Limitations of high-power visible wavelength periodically poled lithium niobate devices due to green-induced infrared absorption and thermal lensing," Conf. on Lasers and Electro-Optics, Presentation CTuD6 (Opt. Soc. Am., Washington, D.C., 1998).

18 Observations made during the course of the SHG and SRO experiments reported here.

CHAPTER 4. CONCLUSION

4.1. Summary of accomplishments

This dissertation presents a model of the electric field periodic poling process in $LiNbO_3$ that predicts poling outcomes. The model is useful as a tool for device design and process development. The model also facilitates the selection of insulator and electrode materials that result in a substantial improvement in the quality of domain structures for periods less than 10 µm.

The model takes as inputs material properties, most of which are already known for $LiNbO_3$. One material property that was needed was the relationship between domain wall velocity and the applied poling field. This relationship was not known for $LiNbO_3$ prior to this research. This dissertation contributes new data relating domain wall velocity to the applied poling field and presents a curve fit describing this relationship.

Based on the model, a reproducible fabrication recipe for 75-mm-diameter, 500-µm-thick wafers of periodically poled $LiNbO_3$ with 6.5-µm-period domains was developed. From these wafers, 53-mm-long, 500-µm-thick samples were obtained for use in 1064 nm second harmonic generation experiments. These samples were over eight times longer than those previously reported in the literature[1].

Quasi-phase-matching (QPM) was achieved over the entire length of these samples and they exhibited the largest normalized conversion efficiency ever reported for bulk cw single-pass second harmonic generation, 8.5%/watt. These samples also produced the highest bulk cw single-pass 532 nm output power ever reported, 2.7 watts, with an internal conversion efficiency of 42%. These samples were also used to produce the first reported cw 532-nm-pumped singly resonant optical parametric oscillator (SRO) based on QPM. This SRO had a threshold below 1W, exhibited 56% quantum efficiency, and tuned from 917 nm to 1266 nm.

4.2. Future work

Despite the accomplishments of this research, a great deal remains to be done to realize the full potential of electric field periodic poling. Extensions of the model are needed to accommodate nonlinear optical materials other than congruent $LiNbO_3$ and to include all the stages of domain kinetics. Efforts to shorten domain periods while maintaining domain duty cycle uniformity over large areas must continue. As ever shorter domain periods are produced and as power handling capability is increased, exciting new devices become possible, and the vision of lasers for displays based on nonlinear optics can be realized.

4.2.1. Modeling

The model presented in this dissertation is based on a set of assumptions that may apply to materials other than $LiNbO_3$, such as $LiTaO_3$ or MgO:$LiNbO_3$. The model should be tested for these candidate materials after their relationships between domain wall velocity and average poling field has been measured. An extension to the model that incorporates anisotropic conductivity can make it useful for materials like KTP and its isomorphs. A further extension to include nonlinear conductivity will aid in the design of electrode structures that mitigate its effects.

The current model is essentially one-dimensional in the sense that domain walls are assumed parallel to the polar axis. Extending the model to two dimensions would provide for tilted domain walls, permitting analysis of the tip propagation and tip termination stages of domain kinetics, and would give insight into the mechanisms behind domain merging. Extending the model further to three dimensions would permit the analysis of two-dimensional electrode structures.

Another useful extension of the model is the inclusion of a time-varying built-in field. This field contributes to the average substrate field and affects domain wall velocity. It also gives rise to back-switching effects that can be used as part of a domain patterning technique. Animation of domain kinetics during electric field periodic poling can serve as a useful tool in teaching the technology.

The model to this point is essentially electrostatic in nature. However, we have seen clearly that there is significant non-electrostatic energy associated with the shape of

domain walls. By including domain wall energy in the model, we can better predict the shape of domain walls for a given electrode and insulator design and can move away from the simple assumption that domain wall velocity is determined solely by the average field in the ferroelectric.

4.2.2. Material

Future work in electric field periodically poled materials will focus on the improvement of sample quality, especially as domain period is decreased, increases in power handling capability, systematic characterization and recipe development for new materials, and improved control of the poling process through new electrode designs.

4.2.2.1. Sample quality

The quality of electric field periodically poled $LiNbO_3$ is determined by the average domain duty cycle and the percent rms duty cycle variation. Typically, the percent rms duty cycle variation increases with decreasing domain period. There are several factors that contribute to duty cycle variation. Among these are defects inherent in the starting material, surface damage during handling, lithographic imperfections, errors in poling waveform design, and insufficient nucleation site density. Surface damage, lithographic imperfections, and problems in poling waveform design are fairly well understood and are easily managed sources of defects. While it appears that domains nucleate in patterns on uniformly electroded samples[2], it is not clear what mechanism in the ferroelectric gives rise to these nuclei. We need to understand the source of these nucleation sites and learn how to eliminate them or they will continue to severely limit process yields

Insufficient nucleation site density along electrode edges can also lead to excessive duty cycle variations. This dissertation has shown that the choice of electrode material can greatly enhance nucleation site density, facilitating the patterning of 6.5-µm-period domains. However, for shorter periods nucleation site density ceases to be the limiting factor on domain pattern quality. As domain nuclei become more closely spaced, they interact to suppress each other's growth. In addition, as the period is decreased, the depth of the fringe fields is decreased and prevents nuclei from attaining the critical size required for tip propagation. One strategy that helps to overcome these limitations is to

reduce substrate thickness to a value on the order of the domain period. Numerous researchers have employed this strategy as they found that they had more success in electric field periodic poling with thin substrates than with thick. An additional advantage of thin substrates is that the magnitude of the fringe fields parallel to the surface of the ferroelectric is proportional to sample thickness. Thinner samples are more likely to avoid dielectric damage and nonlinear conductivity along the ferroelectric-insulator interface than their thicker counterparts.

For thick substrates, I suggest constructing the domain pattern from a series of longer period domain patterns, each poled with its own electrode set in an interleaved fashion. For example, to fabricate a 4-µm-period domain pattern in 500-µm-thick $LiNbO_3$, I recommend interleaving two 8-µm-period electrode patterns. Nucleate and grow domains through the tip termination stage with one electrode pattern. Then repeat the procedure with the second electrode pattern. Finally, grow the domains in the wall propagation stage simultaneously with both electrode patterns. By using two long period patterns, the fringe field depth is increased, allowing the tips of domain nuclei to propagate, and the magnitude of the lateral fringe fields can be kept to a manageable level.

4.2.2.2. Power Handling

Another goal for future work is to increase the power handling capability of electric field periodically poled $LiNbO_3$. In Chapter 3, we saw that as 532-nm output power was increased above ~1.5W, both the power and pointing stability of the output beam decreased. The maximum 532-nm output power that could be obtained was 2.7 watts. The origins of these behaviors must be understood and their causes eliminated to maximize the utility of this material.

4.2.2.3. Materials characterization

Applying the model to new materials will facilitate systematic development of optimized fabrication and poling recipes. Characterization of the material's ferroelectric properties is the first step in this process. An important characteristic that will need to be measured for new materials is the relationship between domain wall velocity and the applied field.

The effect of various electrode materials on nucleation site density should be studied. The time-dependent built-in field, if it exists for that material, should be characterized to aid in poling waveform design.

4.2.2.4. Electrode design

Finally, new electrode designs should be explored to control the location of nucleation sites or to increase the contrast of the poling process. One way to control the location of nucleation sites is to employ electrodes with small protrusions or barbs along their edges. Nuclei will form most readily at the protrusions because of the enhanced fringe fields there.

One way to increase the contrast of the poling process is to employ electrodes split along their length to create additional surface area for the unscreened spontaneous polarization charge created during the wall propagation stage of domain growth. As the domains spread outward from the outermost electrode edges, they also spread inward towards the center of the electrode, increasing the rate at which the field in the ferroelectric is lowered. This method increases the contrast of the poling process while simultaneously improving domain duty cycle control.

4.2.3. New devices

While the main device configuration of this research was bulk single pass second harmonic generation, increases in power handling capability can enable the use of planar waveguides. Planar waveguides provide for confinement in one dimension, and result in increased normalized conversion efficiency that can be used to produce shorter devices. By using the increase in conversion efficiency to reduce device length, temperature and wavelength acceptance bandwidths can be increased. With the recent development of tapering technology[3], alignment of the fundamental source can be achieved with similar tolerances to those needed for the bulk configuration. One promising waveguide technology for increased power handling capability is ZnO indiffusion[4].

Multiple interactions within the same device have recently been reported. We reported third-harmonic generation of 355 nm near-UV light from a single 6.5-μm PPLN grating, where the second harmonic produced from the first grating order was summed

with the fundamental in the third grating order[2]. Bosenberg *et al.* reported a combination OPO and sum-frequency generator implemented on the same piece of $LiNbO_3$ to produce 629 red light.[5] Ross *et al.* reported a first order second harmonic grating and third-order sum-frequency grating together on the same piece of PPLN performed second-harmonic generation of 660 nm radiation and third-harmonic generation of 440 nm light from a 1320 nm laser.[6] By continuing to improve the quality of devices with periods as low as 1 µm, the efficiency of third-harmonic-generation devices can be improved as a result of using a first-order grating for the sum-frequency step.

Perhaps the most exciting possibility for the future of electric field periodic poling is to create domain periods short enough to permit fabrication of a backward wave OPO[7]. The backward wave OPO is a mirrorless and self-tuning device, with the pump wave counter-propagating to the signal and idler waves. Using the Sellmeier equation published by Jundt[8] and taking into account thermal expansion, I calculate that a 756Å first-order grating pumped at 355 nm can be temperature tuned throughout the entire visible spectrum, with the temperature ranging from 150°C to 360°C. Of course, grating harmonics may be employed to achieve quasi-phase-matching, making a fifteenth-order device with a domain period of 1.134 µm easier to realize. Ultimately, the first-order grating could be created in thinned crystals using the electron beam writing technique first reported by Ito, *et al*[9].

4.2.4. Closing comments

Bulk electric field periodic poling technology has evolved at a tremendous rate since its introduction in 1993[10]. By 1997, periodically poled materials had become the key enabling technology behind commercial products, both in the visible[11,12] and in the infrared[13]. I hope that this dissertation will facilitate even more rapid advancement of electric field periodic poling technology and will contribute to the realization of the full potential of quasi-phase-matching.

References for Chapter 4

1 V. Pruneri, R. Koch, P. G. Kazansky *et al*., "49 mW of CW blue light generated by first-order quasi-phase-matched frequency doubling of a diode-pumped 946-nm Nd:YAG laser," Optics Letters **20** (23), 2375-7 (1995).

2 G. D. Miller, R. G. Batchko, M. M. Fejer *et al*., "Visible quasi-phase-matched harmonic generation by electric-field-poled lithium niobate," Proceedings of the SPIE - The International Society for Optical Engineering **2700**, 34-45 (1996).

3 M. H. Chou, M. A. Arbore, and M. M. Fejer, "Periodically-segmented tapered waveguide for mode-size transformation and fundamental mode excitation," in *Conference Edition. Summaries of the Papers Presented at the Topical Meeting, Integrated Photonics Research. 1996 Technical Digest Series. Vol.6* (Opt. Soc. America, Washington, DC, USA, 1996), pp. 506-9.

4 W. M. Young, M. M. Fejer, M. J. F. Digonnet *et al*., "Fabrication, characterization and index profile modeling of high-damage resistance Zn-diffused waveguides in congruent and MgO:lithium niobate," Journal of Lightwave Technology **10** (9), 1238-46 (1992).

5 W. R. Bosenberg, J. I. Alexander, L. E. Myers *et al*., "2.5-W, continuous-wave, 629-nm solid-state laser source," Optics Letters **23** (3), 207-9 (1998).

6 G. W. Ross, N. S. Felgate, W. A. Clarkson, *et al*., "Red and blue light generation by frequency doubling and tripling in periodically poled $LiNbO_3$," Conf. on Lasers and Electro-Optics, Tech. Digest Series, **6**, 384, (Opt. Soc. Am., Washington, D.C., 1998).

7 S. E. Harris, "Proposed backward wave oscillation in the infrared," Appl. Phys. Lett., **9**, 114-115 (1966).

8 D. H. Jundt, "Temperature-dependent Sellmeier equation for the index of refraction, n_e, in congruent lithium niobate," Optics Letters **22** (20), 1553-5 (1997).

9 H. Ito, C. Takyu, and H. Inaba, "Fabrication of periodic domain grating in $LiNbO_3$ by electron beam writing for application of nonlinear optical processes," Electronics Letters **27** (14), 1221-2 (1991).

10 M. Yamada, N. Nada, M. Saitoh *et al*., "First-order quasi-phased matched $LiNbO_3$ waveguide periodically poled by applying an external field for efficient blue second-harmonic generation," Applied Physics Letters **62** (5), 435-6 (1993).

11 A. Harada and Y. Nihei, "Bulk periodically poled MgO-$LiNbO_3$ by corona discharge method," Applied Physics Letters **69** (18), 2629-31 (1996).

12 A. Harada, Y. Nihei, Y. Okazaki *et al*., "Intracavity frequency doubling of a diode-pumped 946-nm Nd:YAG laser with bulk periodically poled MgO-$LiNbO_3$," Optics Letters **22** (11), 805-7 (1997).

13 Aculight Corporation, Model 1100 Tunable Mid-IR PPLN OPO.

APPENDIX A. THE ELECTROSTATICS OF ELECTRIC FIELD PERIODIC POLING

A.1. Introduction

This Appendix presents the derivation of the formulas incorporated in the computer model of the poling process described in Chapter 2. These formulas take advantage of the periodicity and planarity of the periodic poling geometry and only require sampling of the potential on the electrodes and charge density between the electrodes to determine the electric field and potential throughout both the ferroelectric and insulator. The method is non-iterative and does not require mesh algorithms to sample the space in the insulator and ferroelectric. This method is readily implemented on conventional desktop computers without requiring development of compiled software, and its speed permits its use as a design tool. The formulas presented here were used in the work performed for this dissertation to calculate optimum electrode widths, predict domain duty cycles, and optimize poling voltage and poling pulse duration. The ability to compare predictions against experimental results helped in the diagnosis of poling problems.

After defining variables used in the subsequent sections, the formulas used to calculate the electric field and potential at any given location in the ferroelectric or insulator are derived. First given as an infinite Fourier series, they are then converted to discrete Fourier transforms. An optimized procedure for rapidly determining the Fourier coefficients is then described. Next, a method is presented for using those coefficients to rapidly calculate the potential and field anywhere in the ferroelectric or insulator. The field equations are analyzed to provide some sense of the depth of fringe fields and their role in the poling process. In the last section, an equation of domain wall motion is presented which permits the optimization of poling process parameters.

A few words about notation: Italicized characters represent multi-valued quantities such as vectors, matrices, and functions. Plain text characters represent single-valued quantities such as electrode width or insulator thickness. Plain text upper-case Greek

characters represent operators such as the summation symbol. Continuous variables do not change notation when converted to their discrete-space counterparts; their usage can be inferred from context.

Figure A.1 shows the cross-section view for a ferroelectric with a periodic array of thin metal electrodes lithographically defined on its +*z* face and over-coated with a uniform thickness insulator. The potential of the metal electrodes is v_e. The *z*-axis is parallel to the *z*-axis of the original single-domain ferroelectric. The exposed surface of the insulator ($z = t_i$) is held at a uniform covering potential, v_c, typically using an electrolyte contact. The exposed surface of the ferroelectric, the minus *z*-face, ($z = -t_f$) is held at the reference potential, 0 volts, also typically using an electrolyte contact. In the Figure, the direction of the spontaneous polarization P_s is shown for both the un-reversed and reversed regions of ferroelectric. The reversed regions are commonly referred to as domains, although this term generally applies to regions of either sign of spontaneous polarization. The domain duty cycle is defined $DC_d \equiv w_d/\Lambda$, and the electrode duty cycle is defined $DC_e \equiv w_e/\Lambda$.

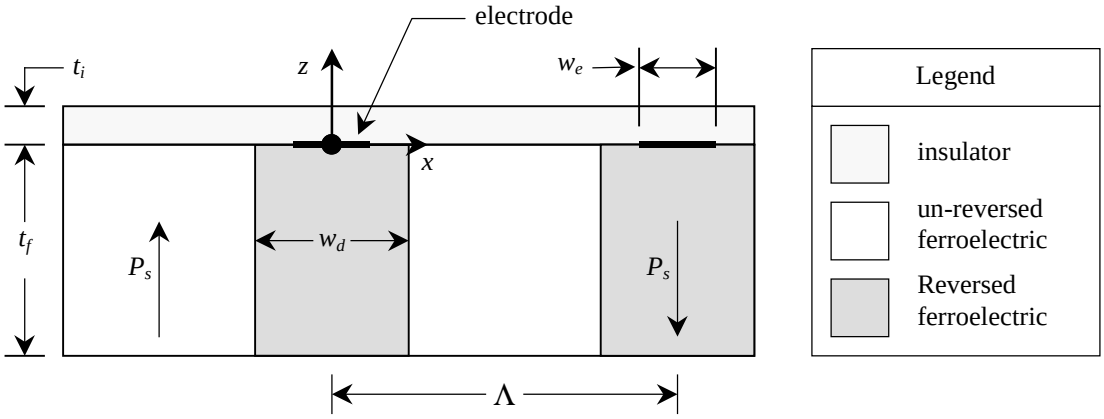

Figure A.1. Poling configuration and variables used to calculate fields and potentials.

A.2. Derivation of Field Equations

We begin with Laplace's equation, since there is no volume charge distribution in the insulator or ferroelectric, thus

$$\frac{\partial^2}{\partial x^2} D_x + \frac{\partial^2}{\partial x^2} D_z = 0 \qquad \text{(A.1)}$$

where D_x is the amplitude of the *x* component of displacement and D_z is the amplitude of the *z* component of displacement. Assuming that the insulator and ferroelectric *z* axes are oriented perpendicular to the ferroelectric-insulator interface, Laplace's equation is written as

$$\varepsilon_x \frac{\partial^2}{\partial x^2}\Phi(x,z) + \varepsilon_z \frac{\partial^2}{\partial z^2}\Phi(x,z) = 0 \tag{A.2}$$

where ε_x is the relative permittivity for *x* polarized fields, ε_z is the relative permittivity for *z* polarized fields (both the insulator and ferroelectric can be anisotropic), and $\Phi(x,z)$ is the two-dimensional potential function. Since both the electrode structure and domain structure are periodic in *x*, $\Phi(x,z)$ is a periodic function in *x*. With the origins of the *x* and *z* axes located in the center of an electrode, the resulting solutions for the insulator and ferroelectric are, satisfying the boundary conditions at $z = -t_f$, $z = 0$, and $z = t_c$, are:

$$\Phi_i'(x',z') = \left[V_0' + \left(v_c' - V_0'\right)\frac{z'}{t_i'}\right] + 2\sum_{n=1}^{\infty} V_n' \cos(k_n x') \frac{\sinh\left[k_n\left(t_i' - z'\right)\right]}{\sinh\left(k_n\, t_i'\right)} \tag{A.3}$$

and

$$\Phi_f'(x',z') = \left(1 + \frac{z'}{t_f'}\right)V_0' + 2\sum_{n=1}^{\infty} V_n' \cos(k_n x') \frac{\sinh\left[k_n\left(t_f' + z'\right)\right]}{\sinh\left(k_n t_f'\right)} \tag{A.4}$$

where the V_n' are the Fourier coefficients to be found. The *i* and *f* subscripts indicate insulator and ferroelectric properties, respectively. The prime notation indicates normalized variables. The normalized distances are

$$x' \equiv \frac{x}{\Lambda};$$

$$z_i' \equiv \frac{z}{\Lambda\sqrt{\varepsilon_{ri}}};$$

$$z_f' \equiv \frac{z}{\Lambda\sqrt{\varepsilon_{rf}}};$$

$$t_i' \equiv \frac{t_i}{\Lambda\sqrt{\varepsilon_{ri}}};$$

$$t_f' \equiv \frac{t_f}{\Lambda\sqrt{\varepsilon_{rf}}}.$$

The dimensionless potentials are

$$v'_c \equiv \; v_c \cdot \text{volt}^{-1};$$

$$\Phi'_i(x',z') \equiv \; \Phi_i\left(\Lambda\, x', \Lambda\sqrt{\varepsilon_{ri}}\; z'\right) \cdot \text{volt}^{-1};$$

$$\Phi'_f(x',z') \equiv \; \Phi_f\left(\Lambda\, x', \Lambda\sqrt{\varepsilon_{rf}}\; z'\right) \cdot \text{volt}^{-1}.$$

The ratios of relative permittivities in the insulator and ferroelectric are

$$\varepsilon_{ri} \equiv \frac{\varepsilon_{zi}}{\varepsilon_{xi}};\; \varepsilon_{rf} \equiv \frac{\varepsilon_{zf}}{\varepsilon_{xf}}.$$

Finally, $k_n \equiv 2\pi n$.

Note that

$$\Phi'_i(x',0) = \Phi'_f(x',0) = v'(x') \equiv V'_0 + 2\sum_{n=1}^{\infty} V'_n \cos(k_n x'), \tag{A.5}$$

indicating that the ferroelectric and insulator potential functions satisfy the boundary condition that they be equal at the ferroelectric-insulator interface.

The potential along the interface is specified only on the electrodes, while surface charge density is specified along the interface between the electrodes. Surface charge density $\rho_s(x)$ equals the difference in displacements normal to the insulator-ferroelectric interface:

$$\rho_s(x) = \frac{\partial}{\partial z}\Phi_f(x,z)\bigg|_{z=0} - \frac{\partial}{\partial z}\Phi_i(x,z)\bigg|_{z=0}. \tag{A.6}$$

Computing the derivatives and expressing the result in non-dimensional coordinates yields

$$\rho'_s(x') = P'_0 + 2\sum_{n=0}^{\infty} P'_n \cos(k_n x') \tag{A.7}$$

where

$$P'_n \equiv Q_n V'_n,$$

$$Q_n \equiv \; k_n\left[\varepsilon_{\mu i}\coth(k_n t'_i) + \varepsilon_{\mu f}\coth(k_n t'_f)\right],$$

$$\rho'_s(x') \equiv \; \frac{\Lambda}{\varepsilon_o \cdot \text{volt}}\rho_s(\Lambda x') + \varepsilon_{\mu i}\frac{v'_i}{t'_i}, \tag{A.8}$$

$\varepsilon_o \equiv$ permittivity of free space,

$\varepsilon_{\mu i} \equiv \sqrt{\varepsilon_{xi}\varepsilon_{zi}}$, and $\varepsilon_{\mu f} \equiv \sqrt{\varepsilon_{xf}\varepsilon_{zf}}$.

A.3. Approximating with Discrete Fourier Transforms

Equations (A.5) and (A.7) can be used to solve for a finite number of Fourier coefficients (V_n') given the boundary conditions specified along the ferroelectric-insulator interface. The factor 2 in Equation (A.5) establishes V' as the Fourier transform of the even, periodic function v'. By truncating the series in Equations (A.5) and (A.7) at some value of N large enough to achieve the desired degree of accuracy, discrete Fourier transform pairs can be written for potential and charge density. Here is the transform pair for potential:

$$v_k' = \sum_{n=0}^{\mathrm{N}-1} V_n' e^{i2\pi nk/\mathrm{N}} = \left[V_0' + 2\sum_{n=1}^{\mathrm{N}/2-1} V_n' \cos\left(2\pi nk/\mathrm{N}\right) + V_{\mathrm{N}/2}'(-1)^k \right], \tag{A.9}$$

$$V_n' = \mathrm{N}^{-1}\left[v_0' + 2\sum_{k=1}^{\mathrm{N}/2-1} v_k' \cos\left(2\pi nk/\mathrm{N}\right) + v_{\mathrm{N}/2}'(-1)^{-1} \right] \tag{A.10}$$

Due to the evenness of v' and V', the value of N Fourier coefficients can be determined using $\mathrm{N}/2+1$ samples uniformly spaced over the interval $0 \le x' \le \frac{1}{2}$. The N coefficients can be found by solving the system of equations

$$\begin{bmatrix} \cos(k_0 x_0') & 2\cos(k_1 x_0') & \cdots & 1 \\ \vdots & \vdots & \ddots & \vdots \\ \cos(k_0 x_{\mathrm{N_e}}') & 2\cos(k_1 x_{\mathrm{N_e}}') & \cdots & (-1)^{\mathrm{N_e}} \\ Q_0\cos(k_0 x_{\mathrm{N_e}+1}') & 2Q_1\cos(k_1 x_{\mathrm{N_e}+1}') & \cdots & (-1)^{\mathrm{N_e}+1} Q_{\mathrm{N}/2} \\ \vdots & \vdots & \ddots & \vdots \\ Q_0\cos(k_0 x_{\mathrm{N}/2}') & 2Q_1\cos(k_1 x_{\mathrm{N}/2}') & \cdots & Q_{\mathrm{N}/2} \end{bmatrix} \begin{bmatrix} V_0' \\ V_1' \\ \vdots \\ V_{\mathrm{N}/2}' \end{bmatrix} = \begin{bmatrix} \mathrm{v_e}' \\ \vdots \\ \mathrm{v_e}' \\ \rho_{s\mathrm{N_e}}' \\ \vdots \\ \rho_{s\mathrm{N}/2}' \end{bmatrix} \tag{A.11}$$

where $\mathrm{v_e}' \equiv \mathrm{v_e} \cdot \mathrm{volt}^{-1}$, $x_n' \equiv n/\mathrm{N}$, $\mathrm{N_e} \equiv \mathrm{floor}\left[\left(\mathrm{DC_e N}+1\right)/2\right]$, and $n = 0, 1, \ldots \mathrm{N}/2$. The floor function returns the largest integer less than or equal to its argument. Using *LU* decomposition with iterative improvement[1], storage for $2(\mathrm{N}/2+1)^2$ floating point numbers is required and $\frac{1}{3}(\mathrm{N}/2+1)^3 + (\mathrm{N}/2+1)^2$ multiplies must be executed.

A.3.1. Convergence

The choice of N depends on the intended use of the Fourier coefficients. If they are to be used to calculate the fringe fields in the vicinity of the electrodes, N must be sufficiently high to capture the spatial harmonics needed for the calculation. Successive increases in N will cause the result to converge for any location in the insulator or ferroelectric with the exception of the edge of the electrode, which is assumed to have zero thickness and therefore gives rise to infinite magnitude fields. In reality, of course, electrodes have some finite thickness, resulting in lower fields than those predicted by the computer model. Additionally, the surrounding insulator permits some charge to flow, resulting in further field reduction.

If only V_0' is needed, for example, to calculate the average field in the ferroelectric for use in domain wall velocity calculations, fewer samples are needed. It is possible to obtain the average field in the ferroelectric to a high degree of accuracy by taking advantage of the convergence behavior of the Fourier coefficients. By fitting the values of V_0' obtained for various values of N with

$$f(N) = g\,N^m + y \tag{A.12}$$

where g, m, and y are fitting parameters, y is a useful estimate of the true value of V_0'. Typically $m \approx -1$.

A.3.2. Optimization

While Equation (A.11) can be used to obtain the Fourier coefficients for a single electrode and domain configuration in a reasonable amount of time on a desktop computer, its use as a tool in electrode and poling waveform design is severely limited. In these applications, the equations are repeatedly solved for an iterative sequence of test designs until convergence is achieved. To substantially shorten computation time, the convolution property of Fourier transforms is next applied, decreasing the number of simultaneous equations to the number of samples on the electrode or insulator, whichever is less. In the worst case, where the electrode duty cycle is 50%, calculation time is reduced by a factor of 8. For an electrode duty cycle of 10%, the reduction is 1000 fold.

Note the following Fourier transform relationships:

$$\begin{aligned} v' &\supset V' \\ \rho' &\supset P' \\ \overline{Q} &\equiv Q^{-1} \\ \overline{q} &\supset \overline{Q} \end{aligned} \tag{A.13}$$

where $\supset$ indicates a forward Fourier transform. Define

$$v'_{e_n} \equiv \left[1-\left(\mathrm{N_e} < n < \mathrm{N}-\mathrm{N_e}\right)\right]\mathrm{v'_e},$$

$$v'_i \equiv v' - v'_e,$$

$$\rho'_{i_n} \equiv \left(\mathrm{N_e} < n < \mathrm{N}-\mathrm{N_e}\right)\left[\varepsilon_{\mu\mathrm{i}}\frac{\mathrm{v'_i}}{\mathrm{t'_i}} - \left[1-\left(\mathrm{N_d} < n < \mathrm{N}-\mathrm{N_d}\right)\right]\frac{2\,\mathrm{P_s}\Lambda}{\varepsilon_\mathrm{o}\cdot\mathrm{volt}}\right], \text{ and}$$

$$\rho'_e \equiv \rho'_s - \rho'_i,$$

where $n = 0\ldots\mathrm{N}-1$ and $\mathrm{N_d} \equiv \mathrm{floor}\left[\left(\mathrm{DC_d N}+1\right)/2\right]$. The sum of the Fourier transforms of the electrode voltage (V'_e) and the voltage along the ferroelectric-insulator interface (V'_i) are related to the sum of the Fourier transforms of the charge density profile on the electrode (ρ'_e) and the charge density profile on the ferroelectric-insulator interface (ρ'_i) by

$$V'_e + V'_i = \overline{Q}\left(F'_e + F'_i\right). \tag{A.14}$$

The voltage on the electrode and charge density profile on the ferroelectric-insulator interface are known and collected on one side:

$$V'_e - \overline{Q}F'_i = \overline{Q}F'_e - V'_i. \tag{A.15}$$

The inverse Fourier transform of both sides is taken:

$$v'_e - \overline{q} * \rho'_i = \overline{q} * \rho'_e - v'_i, \tag{A.16}$$

where $*$ indicates the cyclic convolution of two sequences. By considering only terms on the electrode, an equation solving for the unknown electrode charge density can be obtained:

$$\Pi_e\left\{\overline{q} * \rho'_e\right\} = \Pi_e\left\{v'_e - \overline{q} * \rho'_i\right\} \tag{A.17}$$

where Π_e is a vector operator that produces shortened vectors containing only elements associated with samples on the electrodes.

The matrix operation on the left-hand side of Equation (A.17) gives the contribution to the total convolution $\overline{q} * \left(\rho'_e + \rho'_i\right)$ due only to the charge on the electrode, and the

convolution is executed for only those points on the electrode. Taking advantage of the even symmetry of both $\bar{q}$ and ρ'_s, the following matrix equation can be written:

$$\frac{C}{\mathrm{N}}\begin{bmatrix}\rho'_{e_0}\\ \rho'_{e_0}\\ \vdots\\ \rho'_{e_{\mathrm{N_e}-1}}\\ \rho'_{e_{\mathrm{N_e}}}\end{bmatrix}=\begin{bmatrix}\mathrm{v}'_{\mathrm{e}}-\left(\bar{q}*\rho'_i\right)_0\\ \mathrm{v}'_{\mathrm{e}}-\left(\bar{q}*\rho'_i\right)_1\\ \vdots\\ \mathrm{v}'_{\mathrm{e}}-\left(\bar{q}*\rho'_i\right)_{\mathrm{N_e}-1}\\ \mathrm{v}'_{\mathrm{e}}-\left(\bar{q}*\rho'_i\right)_{\mathrm{N_e}}\end{bmatrix} \tag{A.18}$$

where $C_{a,b}=\bar{q}_{\left[(a-b+\mathrm{N})\bmod \mathrm{N}\right]}+\left(1-\delta_{b,0}\right)\bar{q}_{(a+b)}$, $a,b=0\ldots\mathrm{N_e}$, and where δ is the Kronecker delta function. The solution of Equation (A.18) is a vector of samples of the charge density profile on one half of the electrode, with the other half inferred by symmetry. Joining the electrode charge density profile with the charge density profile for the region between the electrodes produces the vector ρ'_s. Using Equations (A.8) and (A.13), v' is readily obtained. For an electrode duty cycle greater than 50%, an analogous procedure is followed (Equations (A.14) through (A.18)), starting with

$$F'_e+F'_i=Q\left(V'_e+V'_i\right) \tag{A.19}$$

A.4. Calculating potentials and fields

The Fourier coefficients V' are very useful since they enable rapid computation of the potential and field at any location in the ferroelectric or insulator. The potential and field equations are each presented here in a non-dimensional form followed by a conversion to their dimensional form:

$$\Phi'\left(x',z'\right)=\mathrm{v}'_{\mathrm{c}}\frac{z'}{\mathrm{t}'_{\mathrm{i}}}\left(z'>0\right)+\sum_{n=0}^{\mathrm{N}/2}f\left(n\right)V'_n\cos\left(k_n x'\right)\begin{cases}\dfrac{\sinh\left[k_n\left(\mathrm{t}'_{\mathrm{i}}-z'\right)\right]}{\sinh\left[k_n\mathrm{t}'_{\mathrm{i}}\right]}, & 0<z'\le \mathrm{t}'_{\mathrm{i}}\\ \dfrac{\sinh\left[k_n\left(\mathrm{t}'_{\mathrm{f}}+z'\right)\right]}{\sinh\left[k_n\mathrm{t}'_{\mathrm{f}}\right]}, & -\mathrm{t}'_{\mathrm{f}}\le z'\le 0\end{cases} \tag{A.20}$$

$$\Phi\left(x,z\right)=\begin{cases}\Phi'\left(\dfrac{x}{\Lambda},\dfrac{z}{\Lambda\sqrt{\varepsilon_{\mathrm{ri}}}}\right)\cdot\mathrm{volt}, & z>0\\ \Phi'\left(\dfrac{x}{\Lambda},\dfrac{z}{\Lambda\sqrt{\varepsilon_{\mathrm{rf}}}}\right)\cdot\mathrm{volt}, & z\le 0\end{cases} \tag{A.21}$$

$$\vec{E}_i'(x',z') = -\frac{\mathrm{v}_\mathrm{c}'}{\mathrm{t}_\mathrm{i}'}\hat{\mathrm{z}} + \sum_{n=0}^{\mathrm{N}/2}\frac{f(n)V_n'k_n}{\sinh(k_n\mathrm{t}_\mathrm{i}')}\begin{bmatrix}\sin(k_nx')\sinh\left[k_n(\mathrm{t}_\mathrm{i}'-z')\right]\hat{\mathrm{x}}+\\ \cos(k_nx')\cosh\left[k_n(\mathrm{t}_\mathrm{i}'-z')\right]\hat{\mathrm{z}}\end{bmatrix}$$

$$\vec{E}_f'(x',z') = \sum_{n=0}^{\mathrm{N}/2}\frac{f(n)V_n'k_n}{\sinh(k_n\mathrm{t}_\mathrm{f}')}\begin{bmatrix}\sin(k_nx')\sinh\left[k_n(\mathrm{t}_\mathrm{f}'+z')\right]\hat{\mathrm{x}}-\\ \cos(k_nx')\cosh\left[k_n(\mathrm{t}_\mathrm{f}'+z')\right]\hat{\mathrm{z}}\end{bmatrix} \qquad \text{(A.22)}$$

$$\vec{E}'(x',z') = \begin{cases}\vec{E}_i'(x',z'),\ 0<z'\le \mathrm{t}_\mathrm{i}'\\ \vec{E}_f'(x',z'),\ -\mathrm{t}_\mathrm{f}'\le z'\le 0\end{cases}$$

$$\vec{E}(x,z) = \begin{cases}\begin{bmatrix}\sqrt{\varepsilon_{\mathrm{ri}}} & 0\\ 0 & 1\end{bmatrix}\frac{\mathrm{volt}}{\Lambda\sqrt{\varepsilon_{\mathrm{ri}}}}\vec{E}'\left(\frac{x}{\Lambda},\frac{z}{\Lambda\sqrt{\varepsilon_{\mathrm{ri}}}}\right), 0<z\le \mathrm{t}_\mathrm{i}\\ \begin{bmatrix}\sqrt{\varepsilon_{\mathrm{rf}}} & 0\\ 0 & 1\end{bmatrix}\frac{\mathrm{volt}}{\Lambda\sqrt{\varepsilon_{\mathrm{rf}}}}\vec{E}'\left(\frac{x}{\Lambda},\frac{z}{\Lambda\sqrt{\varepsilon_{\mathrm{rf}}}}\right), -\mathrm{t}_\mathrm{f}<z\le 0\end{cases} \qquad \text{(A.23)}$$

where $f(n)\equiv 2-\delta_{n,0}-\delta_{n,\mathrm{N}/2}$. Note that the form of Equations (A.20) and (A.22) is of a Fourier series, indicating that, for a given value of *z*, a vector of potential or field values corresponding to each value of *x* may be obtained in one call to a Fast Fourier Transform.

A.5. Fringe fields

Fringe fields play a significant role in the nucleation and growth of domains. In the vicinity of the edges of electrodes the magnitude of the *z* component of electric field can be many times larger than the average field in the ferroelectric. In addition to the magnitude of the *z* component of the electric field, the depth of fringe fields plays an important role in determining the domain nucleation rate at the edges of electrodes. The nucleation rate is proportional to $\exp(-\Delta W_T/kT)$, where

$$\Delta W_T = W_W + W_D - W_E \qquad \text{(A.24)}$$

and where W_W is the domain wall energy, W_D is the depolarization energy, and W_E is the electrostatic energy in the domain[2,3]. Nuclei located at the edges of electrodes and having a depth much greater than the fringe-field depth will have W_D and W_E very similar to nuclei formed in fringe-field-free regions and therefore will have similar nucleation rates. Nuclei located at the edges of electrodes and having a depth comparable to the fringe-field depth will have substantially higher nucleation rates than nuclei of the same depth formed in fringe-field-free regions. This latter statement is true up to a point; below a characteristic size, domain wall energy begins to dominate the total energy, and acts to

limit the minimum size of domains. The result is that below some characteristic fringe field depth the nucleation rate can be expected to decrease towards that in fringe-field-free regions. In addition to nucleation, domains must be able to grow in order to achieve successful electric field periodic poling. It is possible to achieve nucleation in high fringe-field regions without having sufficient field for the nucleus to grow. The fringe fields need to be deep enough for both nucleation and growth.

The depth of fringe fields is strongly related to the electrode period. Referring to Equations (A.22) and (A.23), the magnitude of the *z* component of the electric field is exponentially related to depth, period, and harmonic:

$$E_z \propto \frac{\cosh\left[\frac{2\pi n}{\Lambda\sqrt{\varepsilon_{rf}}}\left(t_f + z\right)\right]}{\sinh\left[\frac{2\pi n}{\Lambda\sqrt{\varepsilon_{rf}}}t_f\right]}. \tag{A.25}$$

For $\frac{2\pi n}{\Lambda\sqrt{\varepsilon_{rf}}}t_f >> 1$ and $t_f >> -z$,

$$E_z \propto \exp\left(\frac{2\pi n}{\Lambda\sqrt{\varepsilon_{rf}}}z\right). \tag{A.26}$$

The fringe field depth *d* for a given harmonic *n* is defined as the $1/e$ depth and is given by

$$d_n = \frac{\Lambda\sqrt{\varepsilon_{rf}}}{2\pi n}. \tag{A.27}$$

In Equation (A.27), the depth is the greatest for the lowest harmonic and is proportional to the period. In $LiNbO_3$, $d \approx \Lambda/10$.

One tool for visualizing computed fringe fields is the vector plot. Figure A.2 shows the fringe fields for a $LiNbO_3$ sample with the following characteristics:

$$\begin{gathered}\Lambda = 6\,\mu\text{m},\ w_e = 1\,\mu\text{m},\ w_d = 0\,\mu\text{m};\\ t_f = 500\,\mu\text{m},\ \varepsilon_{xf} = 85.2,\ \varepsilon_{zf} = 28.7;\\ t_i = 0.5\,\mu\text{m},\ \varepsilon_{xi} = 3.1,\ \varepsilon_{zi} = 3.1;\\ v_e = 10\,\text{kV}, v_c = 10\,\text{kV};\\ P_s = 0.78\ \text{coul}/\text{m}^2.\end{gathered} \tag{A.28}$$

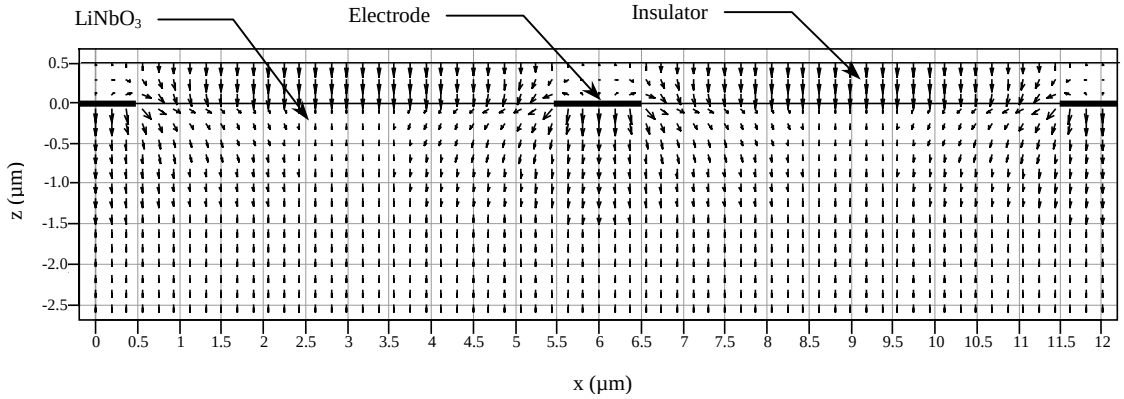

Figure A.2. Vector field plot showing fringe fields for $LiNbO_3$ sample described in Equations (A.28). Square root of field magnitude is used to provide visibility for low field regions.

Note that the polar component of the electric field is strongest under the electrodes and rapidly decays with depth to the average field in the bulk of the ferroelectric. At the edges of the electrodes, the fields develop a strong *x*-component. Strong *x*-directed electric fields near the insulator-ferroelectric interface can lead to breakdown. Note the change in the fringe field characteristics with a domain that has spread out from under the electrode as shown in Figure A.3. All the values set in Equations (A.28) are maintained with the exception that $w_d = 2\,\mu m$.

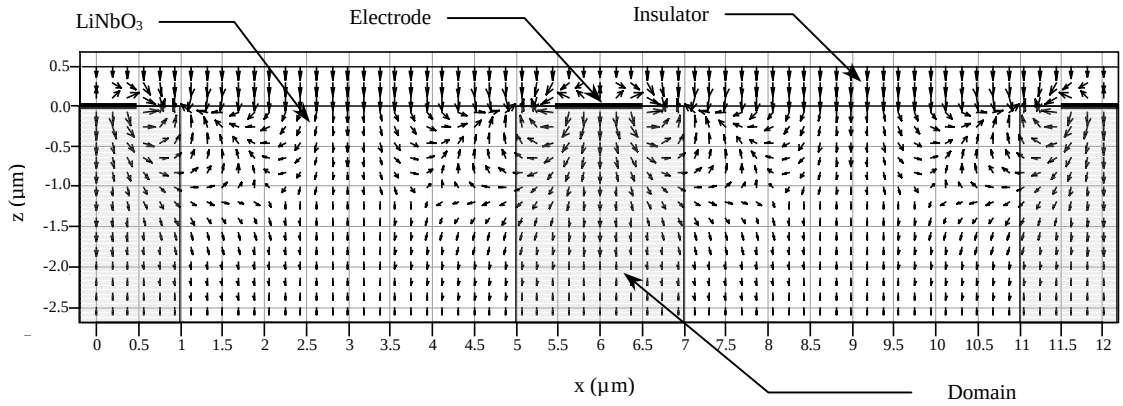

Figure A.3. Vector field plot showing fringe fields for $LiNbO_3$ sample described in Equations (A.28), with 2 μm-wide domains spread 0.5 μm beyond each electrode edge. Eighth root of field magnitude is used to provide visibility for low field regions.

Figure A.3 shows that as domains spread out from under their electrodes, the spontaneous polarization charge deposited on the insulator-ferroelectric interface is large enough to cause the sign of the *z*-component of the electric field to *reverse*. In this example, the reversal extended to a depth of 1 μm, both inside and outside the domain.

The implications of this calculation are significant, since it indicates that domain reversal is proceeding even in the presence of strongly depolarizing fields. Experimental observations that domain walls remain unbent at the insulator-ferroelectric interface support this prediction. The large fields associated with the spreading of domains beyond the electrode edges no doubt lead to some conduction as discussed next, and may reduce or reverse the sign of the fields at the interface. However, more study is required to determine whether the near-surface domains are forming at local fields substantially near the coercive field.

To assess the magnitude of the fringe fields in this example, a plot of the amplitude of the *z*-component of the electric field is shown in Figure A.4. The singularities at the electrode edges are avoided by calculating the field along a line 0.001 µm below the insulator-ferroelectric interface. The number of samples involved in the solution was increased until the peak fields were insensitive to further increases in resolution; 2048 samples were used (N=2048 in Equation (A.23)). While the average field in the ferroelectric far from the electrodes is approximately -18.5 kV/mm, the field under the center of the electrode is over 100 times larger at -2.1 MV/mm and exceeds –50 MV/mm at the electrode edges. Similar values are obtained for the *x*-component of the electric field, shown in Figure A.5. These local fields are over an order of magnitude larger than any known bulk dielectric strength and charge transport is very likely.

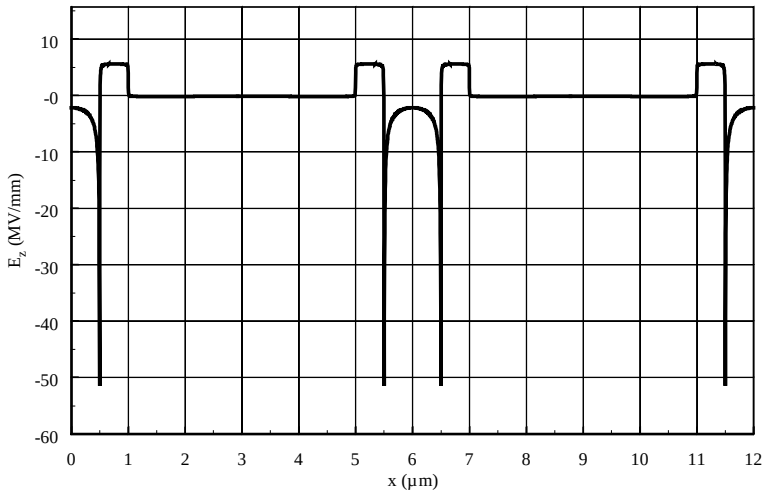

Figure A.4. Amplitude of *z*-component of electric field 1 nm below the insulator-substrate interface for 2-µm-wide domains spreading out from under 1-µm-wide electrodes. The positive field is 5.6 MV/mm at the interface.

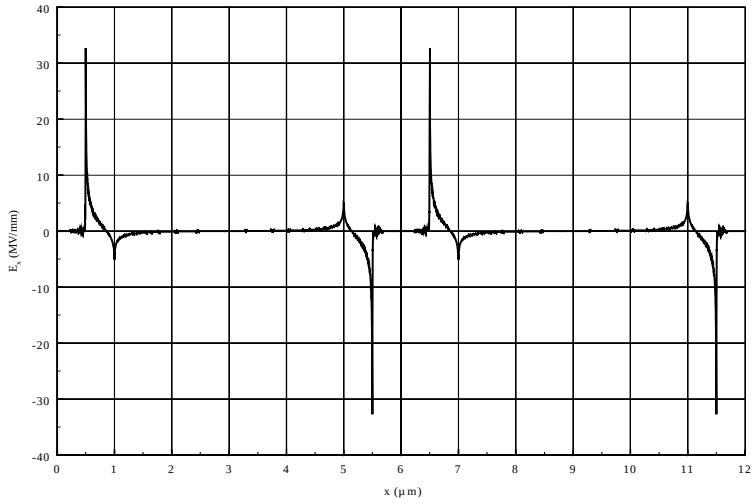

Figure A.5. Amplitude of *x*-component of electric field 1 nm below the insulator-substrate interface for 2-µm-wide domains spreading out from under 1-µm-wide electrodes.

Without having a specific model of charge transport at high fields, we can still assume that some partial screening and charge re-distribution occurs and reduces the magnitude of the fringe fields. Partial screening increases the total charge on the insulator-domain interface and surrounding volume either by removing electrons or adding holes. Electron removal occurs either by transport from the insulator-domain interface to the electrode or by the transport of holes generated at the electrode to the

interface to recombine with electrons there. The addition of holes occurs when they are introduced near the electrodes and migrate to lower field regions where they are trapped. Charge re-distribution conserves the total charge on the insulator-domain interface and surrounding volume. Re-distribution of electrons away from the interface and into the surrounding ferroelectric or insulator, facilitated by nonlinear conductivity, reduces the fringe fields by moving charge away from the interface without annihilating it. Protons in the ferroelectric or insulator can also drift at high fields and contribute to charge re-distribution. Re-distribution of charge leaves the average field deep in the ferroelectric unchanged, while partial screening increases the average field in the substrate. Consequently, charge re-distribution has little or no effect on domain pattern quality, while partial screening can result in excessively spread domains and poor duty cycle uniformity.

A.6. The equation of domain wall motion

A very important use of the Fourier coefficients V' is in the design of electrodes, insulators, and waveforms for electric field periodic poling. Of particular importance is V_0', which provides information about the magnitude of the average field in the ferroelectric in a straightforward manner. As discussed in Chapter 2, the average field in $LiNbO_3$ determines to a large extent the velocity of domain walls. The ability to rapidly calculate the average field as a function of domain duty cycle allows for the optimization of all process parameters. In addition, the ability to calculate ideal poling current as a function of time provides a means for interpreting experimental results.

In the model of electric field periodic poling described in this dissertation, the underlying assertion is that domain wall motion obeys the following relationship

$$DC_d(t) = \frac{2}{\Lambda}\int_0^t \nu\left(V_0'\left(DC_d(\tau)\right)\cdot \mathrm{volt}\cdot \mathrm{t_f}^{-1}\right)d\tau, \tag{A.29}$$

where $DC_d(t)$ is the time dependent domain duty cycle, and ν is the function relating domain wall velocity and average anti-polar field in the ferroelectric, given by Equation XX in Chapter 2. Equation (A.29) provides a means for determining the poling geometry and waveform that causes domain wall motion to essentially stop when the desired duty cycle has been attained.

Equation (A.29) is not intended to fully capture the fine details of domain behavior; instead, it's objective is to deliver an adequate framework for achieving consistent results of good quality periodically-poled material. In attaining this goal, two main assumptions are made. First, it is assumed that domain walls are parallel to the polar axis. Second, it is assumed that the average electric field in the ferroelectric governs domain wall velocity.

A.7. Conclusion

In this Appendix, a means was given for rapidly computing the electric field and potential throughout the ferroelectric and insulator for any given domain duty cycle. An equation of domain wall motion was given, the evaluation of which depends on this computational capability. The equation of domain wall motion is the basis for the model of electric field periodic poling presented in this dissertation, and it provides the means by which process parameters can be optimized.

References for Appendix A

1 Press, William H., Flannery, Brian P., Teukolsky, Saul A., and Vetterling, William T., Numerical Recipes in C. Cambridge University Press, Cambridge, pp. 39-51 (1991).

2 Fatuzzo, E. and Merz, W., Ferroelectricity. North-Holland Publishing Company, Amsterdam, and John Wiley & Sons, Inc., New York, p.236 (1967).

3 Lines, M. E. and Glass, A. M., Principles and applications of ferroelectrics and related materials. Clarendon Press, Oxford, p.108 (1977).

APPENDIX B. EXAMPLE MATHCAD WORKSHEET

This Appendix is an example Mathcad worksheet showing one way to implement the equations presented in Appendix A.

Miscellaneous constants: $\varepsilon_o := 8.854187817 \cdot 10^{-12} \cdot \frac{farad}{m}$ $\mu m := 10^{-6} \cdot m$ $\mu C := 10^{-6} \cdot coul$ $nm := 10^{-9} \cdot m$

Miscellaneous functions:

$$and(a,b) := (a=1) \cdot (b=1) \qquad or(a,b) := 1 - ((a=0) \text{ and } (b=0))$$

$$sv(a,b,c) := submatrix(a,b,c,0,0)$$

Equation (A.8):

$$Q(k, \varepsilon_{\mu i}, \varepsilon_{\mu f}, t'_i, t'_f) := \overrightarrow{\left[k \cdot \left(\varepsilon_{\mu i} \cdot \coth\left(k \cdot t'_i\right) + \varepsilon_{\mu f} \cdot \coth\left(k \cdot t'_f\right)\right)\right]}$$

$$Qinv(k, \varepsilon_{\mu i}, \varepsilon_{\mu f}, t'_i, t'_f) := \overrightarrow{Q(k, \varepsilon_{\mu i}, \varepsilon_{\mu f}, t'_i, t'_f)^{-1}}$$

$$kvec(p) := \left| \begin{array}{l} \text{for } i \in 0..2^{p-1} \\ \quad kp_i \leftarrow i \\ kp_0 \leftarrow 10^{-10} \\ kp \leftarrow stack\left(kp, reverse\left(sv\left(kp, 1, 2^{p-1}-1\right)\right)\right) \\ \text{return } 2 \cdot \pi \cdot kp \end{array} \right.$$

$$\rho'_i(N, N_e, N_d, \rho'_{disp}, P'_s) := \left| \begin{array}{l} \text{for } n \in 0..N-1 \\ \quad ans_n \leftarrow \left| \begin{array}{l} \left(\rho'_{disp} + P'_s\right) \text{ if } \left(n \le N_d\right) \text{ or } \left[n \ge \left(N - N_d\right)\right] \\ \rho'_{disp} \text{ otherwise} \end{array} \right. \text{if } \left(n > N_e\right) \text{ and } \left[n < \left(N - N_e\right)\right] \\ \quad 0 \text{ otherwise} \\ \text{return } ans \end{array} \right.$$

Velocity-field function:

$$E_1 := 19.4 \cdot \frac{kV}{mm} \qquad \nu_1 := 16.3 \cdot \frac{m}{sec} \qquad \delta_1 := 1.29$$

$$E_2 := 15 \cdot \frac{kV}{mm} \qquad \nu_2 := 362 \cdot \frac{\mu m}{sec} \qquad \delta_2 := 3.83$$

$$\nu(E) := \Phi\left(E - E_1\right) \cdot \nu_1 \cdot \exp\left[-\left(\frac{\delta_1 \cdot E_1}{E - E_1}\right)\right] + \Phi\left(E - E_2\right) \cdot \nu_2 \cdot \exp\left[-\left(\frac{\delta_2 \cdot E_2}{E - E_2}\right)\right]$$

Average electric field in crystal. The matrix "ans" also contains the charge density profile and voltage profile on the surface of the crystal.

$E_o(DC_d, p, w_e, \Lambda, t_f, t_i, \varepsilon_{xf}, \varepsilon_{zf}, \varepsilon_{xi}, \varepsilon_{zi}, v_e, v_c, P_s) :=$

$N \leftarrow 2^p$

$w'_e \leftarrow w_e \cdot \Lambda^{-1}$

$w'_d \leftarrow DC_d$

$N_e \leftarrow \text{floor}(0.5 \cdot w'_e \cdot N)$

$N_d \leftarrow \text{floor}(0.5 \cdot w'_d \cdot N)$

$k \leftarrow \text{kvec}(p)$

$\varepsilon_{\mu i} \leftarrow \sqrt{\varepsilon_{xi} \cdot \varepsilon_{zi}}$

$\varepsilon_{\mu f} \leftarrow \sqrt{\varepsilon_{xf} \cdot \varepsilon_{zf}}$

$\varepsilon_{ri} \leftarrow \varepsilon_{zi} \cdot \varepsilon_{xi}$

$\varepsilon_{rf} \leftarrow \varepsilon_{zf} \cdot \varepsilon_{xf}^{-1}$

$t'_i \leftarrow t_i \cdot \left(\Lambda \cdot \sqrt{\varepsilon_{ri}}\right)^{-1}$

$t'_f \leftarrow t_f \cdot \left(\Lambda \cdot \sqrt{\varepsilon_{rf}}\right)^{-1}$

$Q_{inv} \leftarrow \text{Qinv}(k, \varepsilon_{\mu i}, \varepsilon_{\mu f}, t'_i, t'_f)$

$q_{inv} \leftarrow \text{ICFFT}(Q_{inv})$

$v'_c \leftarrow v_c \cdot volt^{-1}$

$v'_e \leftarrow v_e \cdot volt^{-1}$

$\rho'_{disp} \leftarrow \varepsilon_{\mu i} \cdot v'_c \cdot t'^{-1}_i$

$P'_s \leftarrow \frac{\Lambda}{\varepsilon_o \cdot volt} \cdot (-2 \cdot P_s)$

$\rho'i \leftarrow \rho'_i(N, N_e, N_d, \rho'_{disp}, P'_s)$

$bc \leftarrow \text{ICFFT}\left(\overrightarrow{(Q_{inv} \cdot \text{CFFT}(\rho'i))}\right)$

$bc \leftarrow \text{Re}\left[N \cdot \left(v'_e - \text{sv}(bc, 0, N_e)\right)\right]$

for $a \in 0..N_e$

  for $b \in 0..N_e$

    $C_{a,b} \leftarrow q_{inv}((((a-b)+N) \bmod N)) + (1-(b=0)) \cdot q_{inv_{a+b}}$

$\rho'e \leftarrow \text{Re}(\text{lsolve}(C, bc))$

$tmp \leftarrow \text{sv}\left[\rho'i, N_e + 1, N - (N_e + 1)\right]$

$\rho't \leftarrow (\text{stack}(\rho'e, \text{stack}(tmp, \text{reverse}(\text{sv}(\rho'e, 1, N_e)))))$

$P't \leftarrow \text{CFFT}(\rho't)$

$V't \leftarrow \overrightarrow{(Q_{inv} \cdot P't)}$

$v't \leftarrow \text{Re}(\text{ICFFT}(V't))$

$ans \leftarrow \text{augment}(\rho't, \text{augment}(P't, \text{augment}(v't, V't)))$

$ans \leftarrow \text{augment}(ans, k)$

return $ans_{0,3} \cdot volt \cdot t_f^{-1}$

Examples: $E_o\left(25\ \%, 10, 1\cdot\mu m, 6.5\cdot\mu m, 500\cdot\mu m, 0.5\cdot\mu m, 85.2, 28.7, 3.1, 3.1, 10.7\cdot kV, 10.7\cdot kV, 0.78\cdot\frac{coul}{m^2}\right) = 20.896\cdot\frac{kV}{mm}$

$$v\left(E_o\left(25\ \%, 10, 1\cdot\mu m, 6.5\cdot\mu m, 500\cdot\mu m, 0.5\cdot\mu m, 85.2, 28.7, 3.1, 3.1, 10.7\cdot kV, 10.7\cdot kV, 0.78\cdot\frac{coul}{m^2}\right)\right) = 909.349\cdot\frac{nm}{sec}$$

The field in the insulator and ferroelectric can be obtained using the matrix "ans" as the argument "d" in the following.

Field in insulator (1st column is *x*-component, 2nd is *z*-component):

$$E'_i(z', d) := \begin{array}{l} N \leftarrow \text{rows}(d) \\ k \leftarrow sv\left(d^{<4>}, 0, \frac{N}{2}\right) \\ V' \leftarrow sv\left(d^{<3>}, 0, \frac{N}{2}\right) \\ tmp \leftarrow \overrightarrow{\left(k\cdot V'\cdot\frac{e^{-k\cdot z'}}{1-e^{-2\cdot k\cdot t'_i}}\right)} \\ ans^{<0>} \leftarrow \text{Re}\left(\text{IFFT}\left(-j\cdot\overrightarrow{\left[tmp\cdot\left[1-e^{-2\cdot k\cdot\left(t'_i - z'\right)}\right]\right]}\right)\right) \\ ans^{<1>} \leftarrow -\frac{v'}{t'_i}\cdot\frac{c}{} + \text{Re}\left(\text{IFFT}\left(\overrightarrow{\left[tmp\cdot\left[1+e^{-2\cdot k\cdot\left(t'_i - z'\right)}\right]\right]}\right)\right) \\ \text{return } ans \end{array}$$

Field in ferroelectric (1st column is *x*-component, 2nd is *z*-component):

$$E'_f(z', d) := \begin{array}{l} N \leftarrow \text{rows}(d) \\ k \leftarrow sv\left(d^{<4>}, 0, \frac{N}{2}\right) \\ V' \leftarrow sv\left(d^{<3>}, 0, \frac{N}{2}\right) \\ tmp \leftarrow \overrightarrow{\left(k\cdot V'\cdot\frac{e^{k\cdot z'}}{1-e^{-2\cdot k\cdot t'_f}}\right)} \\ ans^{<0>} \leftarrow \text{Re}\left(\text{IFFT}\left(-j\cdot\overrightarrow{\left[tmp\cdot\left[1-e^{-2\cdot k\cdot\left(t'_f + z'\right)}\right]\right]}\right)\right) \\ ans^{<1>} \leftarrow -\text{Re}\left(\text{IFFT}\left(\overrightarrow{\left[tmp\cdot\left[1+e^{-2\cdot k\cdot\left(t'_f + z'\right)}\right]\right]}\right)\right) \\ \text{return } ans \end{array}$$

Total field:

$$E(z,d) := \left| \begin{array}{l} \text{if } \left[\left[(0 < z) \text{ and } \left(z \le t_i \right) \right] \right] \\ \quad \left| \begin{array}{l} tmp \leftarrow E'_i\left(\dfrac{z}{\Lambda \cdot \sqrt{\varepsilon_{ri}}}, d \right) \\ tmp^{\langle 1 \rangle} \leftarrow \dfrac{tmp^{\langle 1 \rangle}}{\sqrt{\varepsilon_{ri}}} \\ \text{return } tmp \cdot \dfrac{m}{\Lambda} \end{array} \right. \\ \text{if } \left[\left(-t_f \le z \right) \text{ and } (z \le 0) \right] \\ \quad \left| \begin{array}{l} tmp \leftarrow E'_f\left(\dfrac{z}{\Lambda \cdot \sqrt{\varepsilon_{rf}}}, d \right) \\ tmp^{\langle 1 \rangle} \leftarrow \dfrac{tmp^{\langle 1 \rangle}}{\sqrt{\varepsilon_{rf}}} \\ \text{return } tmp \cdot \dfrac{m}{\Lambda} \end{array} \right. \\ \text{return } 0 \quad \text{otherwise} \end{array} \right.$$